Fall 2014

Small-signal modeling of grid-supporting inverters in droop controlled microgrids

Jacob Andreas Mueller

Department:

SMALL-SIGNAL MODELING OF GRID-SUPPORTING INVERTERS IN DROOP CONTROLLED MICROGRIDS

by

JACOB ANDREAS MUELLER

A THESIS

Presented to the Faculty of the Graduate School of

MISSOURI UNIVERSITY OF SCIENCE AND TECHNOLOGY

In Partial Fulfillment of the Requirements for the Degree

MASTER OF SCIENCE IN ELECTRICAL ENGINEERING

2014

Approved by

Dr. Jonathan Kimball, Advisor
Dr. Mehdi Ferdowsi
Dr. Pourya Shamsi

ABSTRACT

An approach to modeling externally controlled inverters in droop controlled microgrids is presented. A generic three-phase grid-tied inverter and control system model is derived in synchronous reference frame. The structure of this inverter is intended to be similar in composition to other three-phase inverters whose models and dynamics are well understood. This model is used as a starting point in the development of a more comprehensive model, which is capable of representing the coupling between complex power, bus voltage, and frequency that occurs in a microgrid. This new model is a combination of the generic inverter and an autonomous, grid-forming inverter with a local load. The accuracy of the new model is verified through comparisons of small-signal dynamic predictions, simulations, and experimental results from a microgrid testbed.

The proposed procedure of modifying an existing small-signal model for use in a microgrid system retains the information of the original model while successfully enabling the prediction of dynamic interactions with other generating units in the microgrid. The process is scalable for any number of inverters at the same point of connection, allowing accurate predictions of full system dynamics during distributed control actions, such as black start or grid-resynchronization. Traditional linear control techniques may be used to improve the performance and stability of the microgrid system. This is a demonstrated in an analysis of the systems eigenvalues. Drawing from the insights provided by this analysis, hardware and control parameters are selected to improve the response of the generic inverter.

ACKNOWLEDGMENTS

This project was supported in part by the U.S. Department of Energy SunShot Initiative, award DE0006341 (MARMET Consortium).

I would like to thank my advisor, Dr. Jonathan Kimball, who has been a true mentor to me over the past two years, continuously challenging me to grow professionally and academically. I'd also like to thank the other members of my committee, Dr. Mehdi Ferdowsi and Dr. Pourya Shamsi, who have both played an integral role in my development as a power electronics engineer.

I would not be where I am if it were not for the unyielding support of my mother and father. There are no words that can accurately express my gratitude for the opportunities they have given me.

Finally, to Kelsey, my fiancé and my best friend, thank you for your all of your patience, encouragement, and support.

TABLE OF CONTENTS

LIST OF ILLUSTRATIONS

LIST OF TABLES

1. INTRODUCTION

Microgrid architectures have quickly gained traction as viable options for interfacing distributed generation sources to power distribution networks. A diverse array of control strategies for microgrid operation have been proposed, modeled, and researched. Among these is the conventional P/f, Q/V droop control method for islanded operation. Because most distributed generation sources are interfaced through power-electronic converters, significant research has focused on modeling and control of inverters in islanded microgrids [5, 13, 14, 17, 18], and specific attention has been given to stability [2, 11, 12, 20].

A typical droop-controlled microgrid consists of both grid-forming and grid-supporting (or grid-following) units [23]. Grid-forming units operate autonomously according to their droop controllers, regulating grid frequency and bus voltage based on the active and reactive power needs of the microgrids loads. This strategy allows the inverters to follow the load requirements of the system, provided that they are operating within the bounds of power output limitations. In a microgrid comprised of distributed energy resources, this autonomous load-following operation necessitates some amount of energy storage to decouple the system from the intermittency of the generation sources. For example, a photovoltaic (PV) source operates according to a set of external commands issued by a maximum power point tracker (MPPT). If this source's operating point is not matched to the needs of the load, the efficiency of the generation source degrades considerably. Energy storage allows the needs of the output to be observed, according to the droop equations, independent from the operation of the MPPT. Due to cost and complexity, though, it is unlikely that every generation source will be accompanied by distributed energy storage in a typical microgrid system. PV sources without energy storage to act as a buffer must be interfaced through an inverter that follows the voltage and frequency of the microgrid and operates according to the output conditions set by the MPPT, as opposed to the droop equations that govern the inverters that form the microgrid. Conceptually, the operation of this inverter is identical to that of a grid-connected inverter. The difference lies in the coupling between complex power, bus voltage, and frequency

that naturally exists in a droop-controlled microgrid. In this work, the terms "grid-connected" or "grid-tied" will be reserved for sources connected to stiff electrical grids, while "grid-supporting" will be used to describe sources that are connected to low-inertia microgrids and, therefore, subject to droop-equation-driven uncertainties at the point of connection. In [18], a similar inverter classification system is used, but a further distinction is made according to whether grid-supporting units are able to operate independently in islanded mode. Here, however, this distinction is not made.

Grid-supporting units may broadly be defined to include any generation sources in a microgrid that do not operate under droop control. The PV inverter exporting active power according to a source-specific command is the simplest example. Other devices may be used to regulate bus voltage or otherwise improve power quality, such as volt-VAR compensators or active power filters. Volt-VAR compensators are of particular importance to low-voltage microgrids in which line impedances may be primarily resistive, causing unequal sharing of reactive power between generation sources [2, 3]. While networks of grid-forming units are capable of autonomously regulating frequency and equally sharing active power, microgrid systems often include higher level control in the form of a central controller that issues commands to controllable devices [4, 23]. This is sometimes referred to as secondary control. The microgrid central controller is typically responsible for coordinating advanced microgrid functions. These functions include black-start operation and grid synchronization, both of which involve distributed actions to manipulate bus voltage and frequency [13]. The efficacy of the actions taken by the microgrid central controller is heavily dependent on the dynamic behavior of the grid-support units responding to the controller's commands. There is a need, then, for accurate dynamic models of grid-supporting inverters and methods of predicting the impacts these inverters will have on a microgrid system.

Three phase inverters and their control systems have been thoroughly researched and modeled both when operating in grid-tied [1, 6, 15, 21] and islanded [14, 16, 17] modes. These models can be broken into a set of modular blocks including the output filter, an inner control loop directly controlling inverter output, outer control loop, and a PLL or phase reference generation loop. There is remarkable consistency between existing inverter models in regards to the composition and configuration

of these individual elements. The same current control with cross-coupling removal is used as the innermost loop in [1, 5, 6, 10–12, 14–18, 20]. An LCL filter is used in [1, 14, 16, 17, 21] while an LC filter is used in [2, 10, 18]. The same synchronous-reference-frame-based PLL is used in [1, 6, 10, 14–18]. These commonly used building blocks together constitute a baseline inverter structure around which outer loops are constructed according to the operational goals of the inverter. Each individual block is an avenue of research in which countless innovations have been proposed to improve efficiency or to further specialize an inverter for a particular function. Here, the most common of these elements are combined to provide a general purpose grid-tied inverter. This inverter is then used as a test case to demonstrate a process of modifiying an existing grid-tied model such that it accurately describes small-signal dynamics for operation in a droop controlled microgrid.

The remainder of this thesis is structured as follows. First, the derivation of a generic grid-tied system is given and the adjustments it requires to represent a grid-supporting system in a microgrid are outlined. This involves a discussion of the bus voltage calculation used in the model of the grid-forming inverter that serves as the backbone of the droop-controlled microgrid, since the bus voltage and frequency are the points of connection through which the models are combined. Next, the accuracies of both the grid-tied and grid-supporting models are validated through comparisons of model predictions, simulations, and results of hardware experiments. Finally, the models are used to analyze the relationships between control parameters and system performance, specifically in regards to poorly-damped resonances that may affect microgrid stability. These relationships are exploited to maximize the damping of problem modes, and the performance of the experimental system is shown to improve significantly as a result.

2. DERIVATION OF MATHEMATICAL MODELS

In order to accurately represent the responses of grid-supporting units in low-inertia microgrid systems, two models of inverter-based distributed generation sources and their control systems are considered. First, a model is derived for a three-phase grid-supporting inverter capable of sourcing active or reactive power at an arbitrary power factor. This inverter system is intended to be as generic as possible. The functions of a grid-supporting inverter are diverse, and this inverter is intended to represent as many of them as possible. Next, a model of a grid-forming unit operating in droop control at a nominal load is used to provide insight into the variations in grid frequency and bus voltage that may result from changes in the output power of a grid-support unit connected to the same bus. These two inverters together constitute a minimal implementation of an islanded microgrid system. The dynamic predictions of the linearized grid-support model are shown to be accurate both when grid parameters are known and fixed, as is the case when connecting to a stiff grid, and also when parameters are set by a low-inertia generation source. Accuracy is verified through comparison to simulation and experimental results of transient changes in commanded active and reactive power. An eigenvalue analysis is then performed for the linearized models to determine important changes resulting from parameter variations that may impact system stability. Using this process, controller gains or physical parameters may be determined to ensure compatibility with the characteristic sensitivities of a droop-controlled microgrid.

2.1. MODELING GRID-SUPPORT UNIT

The grid-supporting inverter fits the control and hardware topology most typical of three-phase voltage source inverters used to interface distributed generation sources. It is intended to fill a variety of roles and can export power at an arbitrary power factor as commanded, both when connected to a stiff grid and to a low-inertia microgrid. The full system is shown in Figure 2.1 with the output of the inverter connected to a stiff grid. The model is derived in a synchronously rotating reference frame, relying on a phase angle calculated by a PLL. The innermost loop controls the

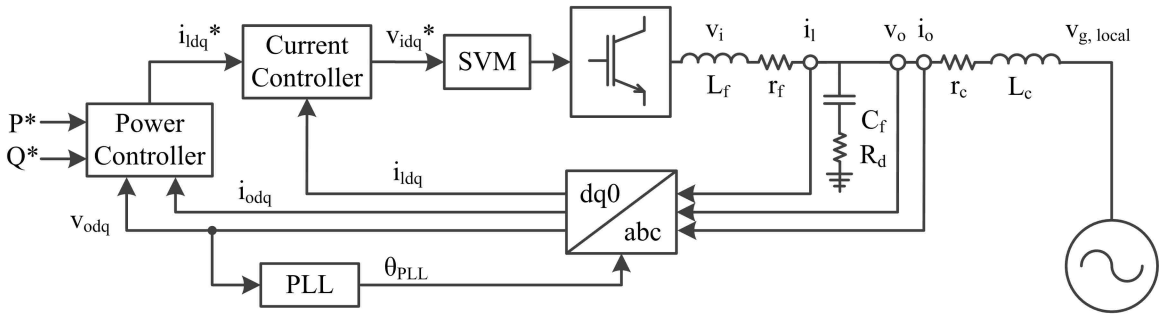

Figure 2.1 Grid-supporting inverter system overview

filter inductor current, following current references and removing cross coupled terms caused by the reference frame transformation. The outer loop provides the current references corresponding to commanded active and reactive power setpoints. The output of the inverter is connected to the rest of the microgrid through an LCL filter. The following is a breakdown of the individual blocks of the system and development of the state-space model from the nonlinear differential equations.

2.1.1. LCL Filter. The LCL filter circuit equations are derived in the synchronous reference frame. On the grid side, voltage $v_{gdq,local}$ refers to the grid voltage as described according to the locally calculated reference angle, which is used in the reference frame transformation. This is discussed further in the PLL subsection. The LCL filter, shown in Figure 2.1 as a single phase equivalent circuit, consists of filter inductor L_f, filter capacitor C_f, and coupling inductor L_c. The coupling inductor may be a discrete component, or may represent the inductance of an isolating transformer, as in [15]. The model includes the series resistances of the filter and coupling inductors, r_f and r_c, respectively. The resonance of the filter is passively damped by resistor R_d. This resistor also represents the series resistance of the capacitors, which is much smaller than the damping resistance. The equations pertaining to the LCL filter are:

$$\dot{i}_{ld} = \frac{1}{L_f}\Big(v_{id} - v_{od} - r_f i_{ld}\Big) + \omega_g i_{lq} \tag{1}$$

$$\dot{i}_{lq} = \frac{1}{L_f}\Big(v_{iq} - v_{oq} - r_f i_{lq}\Big) - \omega_g i_{ld} \tag{2}$$

$$\dot{i}_{od} = \frac{1}{L_c}\Big(v_{od} - v_{gd,\,local} - r_c i_{od}\Big) + \omega_g i_{oq} \tag{3}$$

$$\dot{i}_{oq} = \frac{1}{L_c}\Big(v_{oq} - v_{gq,\,local} - r_c i_{oq}\Big) - \omega_g i_{od} \tag{4}$$

$$\dot{v}_{od} = R_d\Big(\dot{i}_{ld} - \dot{i}_{od}\Big) + \frac{1}{C_f}\Big(i_{ld} - i_{od}\Big) + \omega_g v_{oq} \tag{5}$$

$$\dot{v}_{oq} = R_d\Big(\dot{i}_{lq} - \dot{i}_{oq}\Big) + \frac{1}{C_f}\Big(i_{lq} - i_{oq}\Big) + \omega_g v_{od} \tag{6}$$

2.1.2. Current Controllers. The current controller is perhaps the most generic aspect of the inverter model. The function of the controllers is to ensure that the filter current follows the reference current i^*_{ldq}. At the output of the controllers, cross-coupled terms are removed and the d- and q-axis voltage commands are sent to a space vector modulation (SVPWM) function, which calculates appropriate duty ratios. In this work, the averaged switch modeling technique is used to approximate the output of each phase leg as a continuous voltage source. This is a viable approximation as long as the switching frequency is high compared to the dynamics of the control system and considerations are given to minimizing the effects of switch dead-time in the modulation strategy. The structure of the controllers are shown as Figure 2.2, and the equations that describe their behavior are:

$$\dot{\gamma}_d = i^*_{ld} - i_{ld} \tag{7}$$

$$\dot{\gamma}_q = i^*_{lq} - i_{lq} \tag{8}$$

$$v_{id} = kp_{id}\left(\dot{\gamma}_d\right) + ki_{id}\gamma_d - \omega_n L_f i_{lq} \tag{9}$$

$$v_{iq} = kp_{iq}\left(\dot{\gamma}_q\right) + ki_{iq}\gamma_q + \omega_n L_f i_{ld} \tag{10}$$

2.1.3. Power Controllers. While there is consistency in the PLL, current controllers, and filters used in grid-tied inverters, there is considerable diversity in the outermost control loops. These loops are typically designed to fit the specific purpose of the inverter. Regardless of their higher level objectives, their outputs are d- and q-axis current commands, which are used as reference values by the current controllers. For generality, both active and reactive power must be controlled at arbitrary command values. Commanded values P^* and Q^* are exogenous inputs that originate from a control source beyond the scope of the local model. The structure

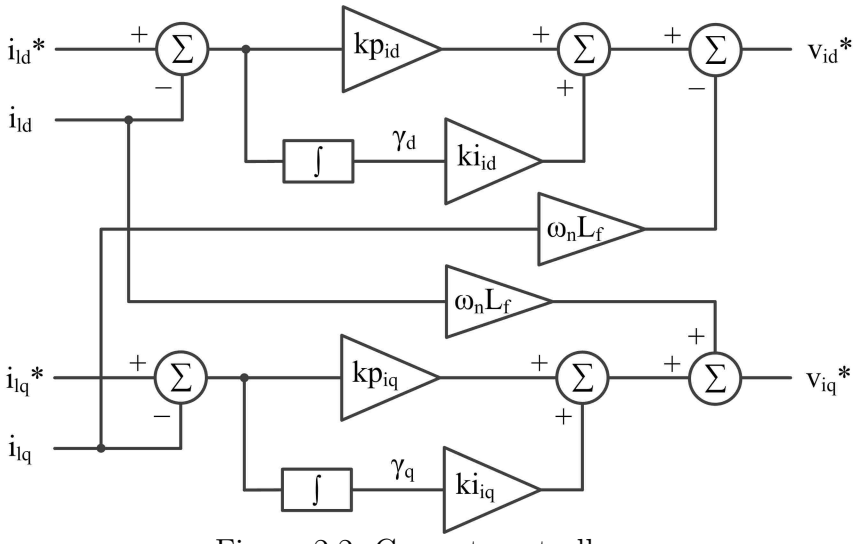

Figure 2.2 Current controllers

is shown in Figure 2.3. Because the d-axis voltage is controlled to 0 by the PLL, the q-axis current is associated with active power P, and the d-axis current is associated with reactive power Q. Instantaneous active and reactive power p and q are calculated from the output voltage and current and filtered using a low-pass filter. The cutoff frequency ω_c is much less than the fundamental frequency of the grid. Power command inputs P^* and Q^* are compared to P_{avg} and Q_{avg} and the current reference is calculated. The power calculation and current reference generation equations are:

$$p = \frac{3}{2}\Big(v_{od}i_{od} + v_{oq}i_{oq}\Big) \tag{11}$$

$$q = \frac{3}{2}\Big(v_{oq}i_{od} + v_{od}i_{oq}\Big) \tag{12}$$

$$\dot{P}_{avg} = \omega_c\Big(p - P_{avg}\Big) \tag{13}$$

$$\dot{Q}_{avg} = \omega_c\Big(q - Q_{avg}\Big) \tag{14}$$

$$\dot{\phi}_q = P^* - P_{avg} \tag{15}$$

$$\dot{\phi}_d = Q^* - Q_{avg} \tag{16}$$

$$i^*_{ld} = kp_Q\phi_Q + ki_Q\dot{\phi}_d \tag{17}$$

$$i^*_{lq} = kp_P\phi_P + ki_P\dot{\phi}_q \tag{18}$$

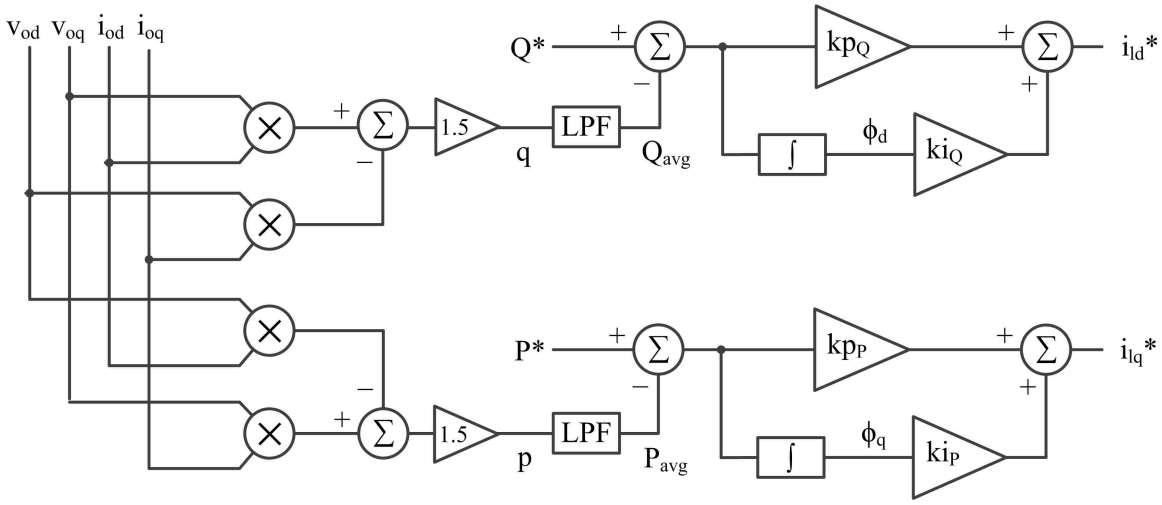

Figure 2.3 Power controllers

Variables ϕ_q and ϕ_d in equations (17) and (18) are states relating to the integrators of the controllers.

2.1.4. PLL and Reference Frame Transformations. A standard SRF-PLL is used to track the frequency and phase angle of the grid. This is shown in Figure 2.4. The PLL regulates the d-axis component of the capacitor voltage to 0.

$$\dot{\phi}_{PLL} = -v_{od} \tag{19}$$

$$\omega_{PLL} = kp_{PLL}\left(\dot{\phi}_{PLL}\right) + ki_{PLL}\phi_{PLL} \tag{20}$$

$$\theta_{PLL} = \dot{\omega}_{PLL} \tag{21}$$

$$\dot{\delta} = \omega_g - \omega_{PLL} \tag{22}$$

Phase angle θ is used in the reference frame transformation, ϕ_{PLL} is an integrator state, and δ represents the difference between the actual grid phase angle and the value calculated by the PLL. This difference must be accounted for in equations relating parameters calculated in the inverter's local reference frame to those in the global reference frame. In grid-tied operation, the global reference frame is set by the grid. The transformation used to refer quantities derived in one reference frame to another is given by the following equation using a dummy variable a_{dq}. This transformation is commonly used in modeling inverters and synchronous machines [14, 19, 22].

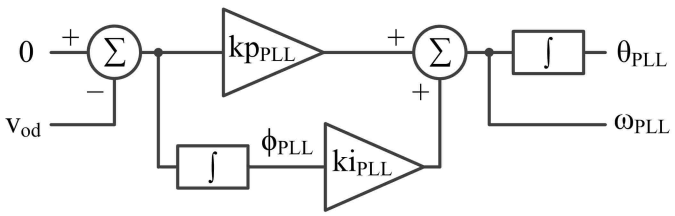

Figure 2.4 PLL controller

$$T_{global}^{local} = \begin{bmatrix} \cos\delta & -\sin\delta \\ \sin\delta & \cos\delta \end{bmatrix}$$

$$a_{dq,\,local} = T_{global}^{local} a_{dq,\,global} \tag{23}$$

2.1.5. Full Model and Linearization. These blocks may be combined into a set of nonlinear equations containing 14 states and 5 inputs. The states and inputs of the system are:

$$u = \begin{bmatrix} P^* & Q^* & v_{gd,\,global} & v_{gq,\,global} & \omega_g \end{bmatrix}^T \tag{24}$$

$$x = \begin{bmatrix} \delta & P_{avg} & Q_{avg} & \phi_d & \phi_q & \gamma_d & \gamma_q \\ & v_{od} & v_{oq} & i_{ld} & i_{lq} & i_{od} & i_{oq} & \phi_{PLL} \end{bmatrix}^T \tag{25}$$

The full nonlinear model consists of state equations (1), (2), (3), (4), (5), (6), (7), (8), (13), (14), (15), (16), (19), and (22). This system is in the form:

$$\dot{x} = F(x, u) \tag{26}$$

In the case of the grid-tied system, inputs $v_{gdq,\,global}$ and ω_g are fixed by the grid itself. Setting the command inputs P^* and Q^* to their appropriate nominal values provides a constant input u_0. Substituting values for the control gains and physical parameters allows the nonlinear system to be solved for its equilibrium points. These points x_0 are the steady state values around which the system will be linearized. The system is perturbed around x_0 and u_0, and the resulting equations are expressed as Taylor series expansions, ignoring higher order terms.

$$\dot{x}_0 + \dot{\tilde{x}} = F\big((x_0 + \tilde{x}), (u_0 + \tilde{u})\big) \tag{27}$$

$$\dot{x}_0 + \dot{\tilde{x}} = F(x_0, u_0) + J_F(\tilde{x})\Big|_{\substack{x_0 \\ u_0}} + J_F(\tilde{u})\Big|_{\substack{x_0 \\ u_0}} \tag{28}$$

$$\dot{\tilde{x}} = J_F(\tilde{x})\Big|_{\substack{x_0 \\ u_0}} + J_F(\tilde{u})\Big|_{\substack{x_0 \\ u_0}} \tag{29}$$

$$\dot{\tilde{x}} = A\tilde{x} + B\tilde{u} \tag{30}$$

Equations (28) and (29) use the Jacobian, denoted J, of the nonlinear system in (26). Equation (30) is the small-signal model for the grid-tied inverter around operating point x_0, u_0. This approach is applicable to a grid-supporting inverter as well, due to the inclusion of small-signal inputs for $\tilde{v}_{gdq,\,global}$ and $\tilde{\omega}_g$, which can be used to describe the behavior of an islanded microgrid. To predict the grid-supporting unit's reactions to these variations, the exact nature of the changes in input must be described. To this end, a grid-forming unit must be considered.

2.2. INFLUENCE OF GRID-FORMING UNIT

The grid-forming unit considered is an autonomous, islanded inverter operating in both frequency and voltage droop control. The small-signal model of this system is described as a single autonomous unit in [17] and as one of multiple participating in a full microgrid in [16].

2.2.1. Droop Controllers. The inverter and control system structure differs from the grid-supporting unit only in regards to the outermost control loop. Where the grid-supporting inverter controls output power in this loop, the grid-forming inverter regulates both grid voltage and frequency according to its droop equations. The droop controllers are shown in Figure 2.5, and the equations for these controllers are given in equations (31) through (34).

$$\omega^* = \omega_n - nP_{avg} \tag{31}$$

$$v_{oq}^* = v_{oq,\,n} - mQ_{avg} \tag{32}$$

$$\dot{\phi}_d = \omega_{PLL} - \omega^* \tag{33}$$

$$\dot{\phi}_q = v_{oq}^* - v_{oq} \tag{34}$$

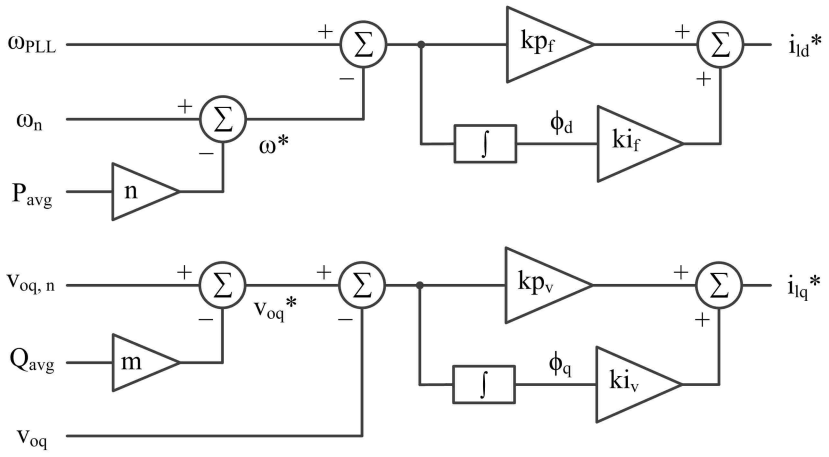

Figure 2.5 Droop controllers

Parameters n and m in equations (31) and (32) are the droop constants. These values determine the magnitude of the changes in frequency and bus voltage that will occur as a response to changes in complex power.

2.2.2. Bus Connection. The output of the grid forming unit is connected to a microgrid bus. Other connections at this point typically include a local load and a distribution line leading to another bus. In islanded inverter modeling, the voltage at this point is often calculated using a virtual resistor to ground. The equations for this node voltage are:

$$v_{bd,\,global} = r_n\Big(i_{od,\,global} + i_{d,\,line} - i_{d,\,load}\Big) \tag{35}$$

$$v_{bq,\,global} = r_n\Big(i_{oq,\,global} + i_{q,\,line} - i_{q,\,load}\Big) \tag{36}$$

Parameter r_n in equations (35) and (36) is the virtual resistance. Line and load currents are always calculated in the global reference frame, and $i_{odq,\,global}$ is the output current of the local grid-forming unit after being transformed into the global reference frame. By altering these equations, the presence of a locally connected grid-supporting unit may be reflected in the system. This simply involves adding the grid-supporting unit connection and applying KCL. Including the newly added external d- and q-axis currents, $i_{dq,\,ext}$, the bus voltage equations are:

$$v_{bd,\,global} = r_n\Big(i_{od,\,global} + i_{d,\,line} + i_{d,\,ext} - i_{d,\,load}\Big) \tag{37}$$

$$v_{bq,\,global} = r_n\Big(i_{oq,\,global} + i_{q,\,line} + i_{q,\,ext} - i_{q,\,load}\Big) \tag{38}$$

2.2.3. Full System and Linearization. Currents $i_{dq,\,ext}$ are generated externally by the grid-supporting unit and are in the global reference frame. Since these values are not present in the autonomous grid-forming system they must be treated as inputs. Considering $v_{bdq,\,global}$ and ω_{PLL} as outputs, the resulting nonlinear system is described by:

$$\dot{x}_{frm} = F_{frm}\big(x_{frm}, u_{frm}\big) \tag{39}$$

$$y_{frm} = G_{frm}\big(x_{frm}, u_{frm}\big) \tag{40}$$

$$u_{frm} = \begin{bmatrix} i_{d,\,ext} & i_{q,\,ext} \end{bmatrix}^T \tag{41}$$

$$y_{frm} = \begin{bmatrix} v_{bd,\,global} & v_{bq,\,global} & \omega_{PLL} \end{bmatrix}^T \tag{42}$$

$$\begin{aligned} x_{frm} = \big[&\delta \quad P_{avg} \quad Q_{avg} \quad \phi_d \quad \phi_q \quad \gamma_d \quad \gamma_q \\ &v_{od} \quad v_{oq} \quad i_{ld} \quad i_{lq} \quad i_{od} \quad i_{oq} \quad \phi_{PLL} \quad i_{d,\,load} \quad i_{q,\,load}\big]^T \end{aligned} \tag{43}$$

Setting inputs to 0, the nonlinear equations may be solved for the equilibrium point at which the grid-forming unit is satisfying the power requirements of its local load. The system is linearized at this point, $x_{0,\,frm}$, according to the same procedure used for the grid-supporting unit in Section 2.1.5. This results in a small-signal model in the traditional state-space form. If only the inputs and outputs are of interest, the system may represented by a 2-input, 3-output transfer matrix, as shown in (44).

$$\tilde{y}_{frm}(s) = H(s)\tilde{u}_{frm}(s) = \begin{bmatrix} H_{i_d}^{\omega}(s) & H_{i_q}^{\omega}(s) \\ H_{i_d}^{v_d}(s) & H_{i_q}^{v_q}(s) \\ H_{i_q}^{v_d}(s) & H_{i_d}^{v_q}(s) \end{bmatrix} \tilde{u}_{frm}(s) \tag{44}$$

Matrix $H(s)$ in equation (44) is composed of 16^{th} order transfer functions, and variable s is used as the Laplace operator. This representation is useful when considering the grid-forming unit as an unchangable system, to which the grid-supporting unit will be added. In this way, matrix $H(s)$ can be used to represent a system of controllable plants that respond to commands sent to the grid-supporting unit. In

the following discussion, the grid-forming model will be treated as a linearized state-space model, but this transfer matrix form is an equally valid representation. The state-space form, though, allows the two models to be combined without significant modifications.

2.3. COMBINATION OF INVERTER MODELS

The grid-supporting and grid-forming models may combined into a single, all-encompassing model. The described system is shown in Figure 2.6. The combined model reflects all dynamic interactions between the two inverters. First deriving the models and then combining them allows their individual design concerns to be observed before considering their interactions. This further has the benefit of decreasing the amount of time spent solving nonlinear differential equations. If the models were derived together as a single nonlinear system, all 31 equations would need to be solved simultaneously to determine the linearization point. In the design process, a new numerical solution would need to be found every time a control gain or physical parameter is adjusted. These calculations are difficult and computationally intensive, so it is preferable to keep the models separate.

To build a combined model, the grid-forming unit must first be developed on its own, as described above, supplying power to its local loads. The frequency and bus voltage at this inverter's steady state operating point are then used in the linearization of the grid-support model. This is the same procedure as for a stiff grid, except that

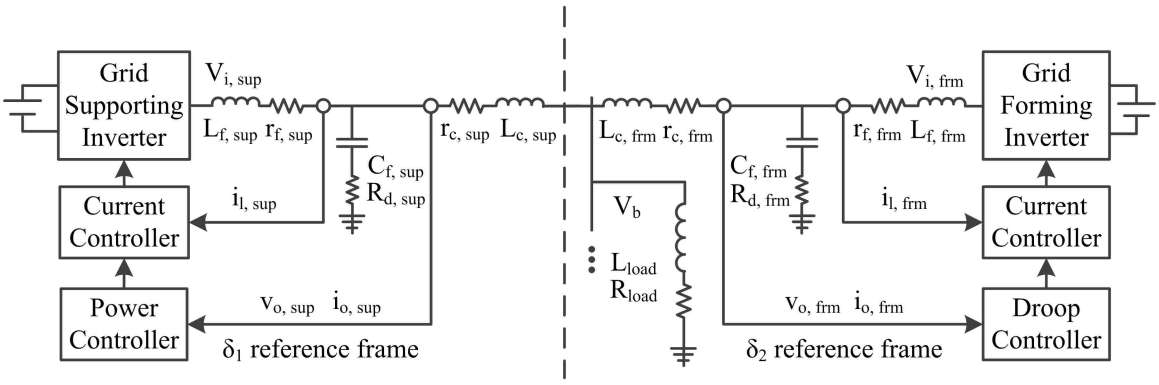

Figure 2.6 Grid-supporting and grid-forming systems

the frequency and voltage values used in linearization are set by the load and droop constants. At this point the models are in the state-space form shown in Figure 2.7, and described in equations (45) and (46). For clarity, subscripts *sup* and *frm* are used indicate whether the matrices and state vectors correspond to supporting unit or forming unit models, respectively.

$$\dot{\tilde{x}}_{sup} = A_{sup}\tilde{x}_{sup} + B_{sup}\tilde{u}_{sup} \qquad \tilde{y}_{sup} = C_{sup}\tilde{x}_{sup} + D_{sup}\tilde{u}_{sup} \tag{45}$$

$$\dot{\tilde{x}}_{frm} = A_{frm}\tilde{x}_{frm} + B_{frm}\tilde{u}_{frm} \qquad \tilde{y}_{frm} = C_{frm}\tilde{x}_{frm} + D_{frm}\tilde{u}_{frm} \tag{46}$$

The states of the supporting unit are the same as for the model operating in grid-tied operation, though previously no subscript was used. The combined model has all states of both grid-supporting and grid-forming models. The full A matrix may be combined using the individual models' A matrices as block diagonal terms. Since the inputs of the grid-forming model are the outputs of the grid-support model, the off-diagonal elements of the new A matrix must be populated from the independent B, C, and D matrices. The same is true of the inputs of the grid-support model, excluding exogenous control inputs P^* and Q^*. This is done as follows:

$$\tilde{x}_{full} = \left[\begin{array}{c} [\tilde{x}_{sup}]^{14\times1} \\ \hline [\tilde{x}_{frm}]^{17\times1} \end{array}\right] \tag{47}$$

$$\tilde{u}_{all} = \left[\begin{array}{c} [\tilde{u}_{sup}]^{5\times1} \\ \hline [\tilde{u}_{frm}]^{2\times1} \end{array}\right] = \left[\begin{array}{c} [\tilde{u}_{ext}]^{2\times1} \\ \hline [\tilde{u}_{int}]^{5\times1} \end{array}\right] \tag{48}$$

$$B_{all} = \left[\begin{array}{c|c} [B_{sup}]^{14\times5} & 0 \\ \hline 0 & [B_{frm}]^{17\times2} \end{array}\right] = \left[\begin{array}{c|c} \left[B_{ext}\right]^{31\times2} & \left[B_{int}\right]^{31\times5} \end{array}\right] \tag{49}$$

$$D_{sup} = \left[\begin{array}{c|c} [D_{ext}]^{2\times2} & [D_{int}]^{2\times3} \end{array}\right] \tag{50}$$

$$A_{full} = \left[\begin{array}{c|c} [A_{sup}]^{14\times14} & 0 \\ \hline 0 & [A_{frm}]^{17\times17} \end{array}\right] + \left[\begin{array}{c} [B_{int}]^{31\times5} \end{array}\right] \left[\begin{array}{c|c} [D_{frm}C_{sup}]^{3\times14} & [C_{frm}]^{3\times17} \\ \hline [C_{sup}]^{2\times14} & [D_{int}C_{frm}]^{2\times17} \end{array}\right] \quad (51)$$

$$\dot{\tilde{x}}_{full} = A_{full}\tilde{x}_{full} + B_{ext}\tilde{u}_{ext} \quad (52)$$

Equation (52) is the final small-signal model of the two inverter system. The inputs $\tilde{u}_{ext}$ are control inputs P^* and Q^*. Equation (51) eliminates the inputs that can be calculated internally from the states of the combined system, effectively closing the loop around the inverters. This is shown graphically in Figure 2.8.

This calculation is intended to be done numerically after the individual models are linearized, allowing the linearization steps to be performed separately. The models can also be combined before they are linearized, but this approach requires a system of 31 nonlinear equations to be solved for the desired steady state operating point. Table 2.1 shows a comparison of calculation times for the grid-forming, grid-supporting, and combined nonlinear system solutions using different implicit ODE solvers.

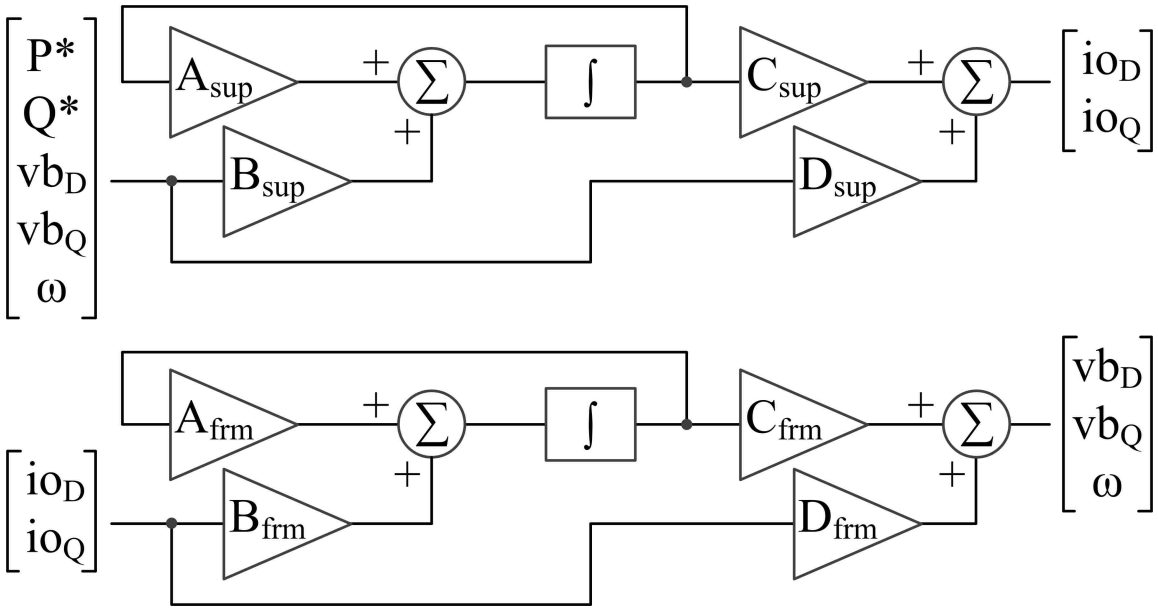

Figure 2.7 Grid-supporting and grid-forming models in state space form

These calculations were performed in MATLAB on three different PCs of various performance calibers. Computers A and B both run 64-bit operating systems (and 64-bit MATLAB). Computer A is designed for higher performance and has a 3.9 GHz CPU and 32 GB of RAM, where computer B has a 2.67 GHz CPU with 8 GB of RAM. Computer C is a laptop running a 32-bit operating system. Its hardware includes a 2.67 GHz CPU and a modest 4 GB of RAM. On all three machines, the calculation time for the combined system equations was orders of magnitude greater than the sum of the calculation times required for the individual inverter systems.

While the difference in calculation times is minimal for a single operating point, it becomes an important factor when extending this process to multiple paralleled grid-support units. Using the same procedure as described above, a combined model can be derived for n grid-supporting inverters connected to the bus at the grid-forming unit's output. Each grid-supporting unit may be added unchanged, and the only modification needed at the grid-forming unit is the inclusion of d- and q-axis current inputs from each inverter. Since the grid-supporting inverters have the same point of connection they can all use the same voltage and frequency values as inputs. Each grid-supporting inverter may be designed individually, and changes made to one will not affect the individual models of the others. Were the full system to be

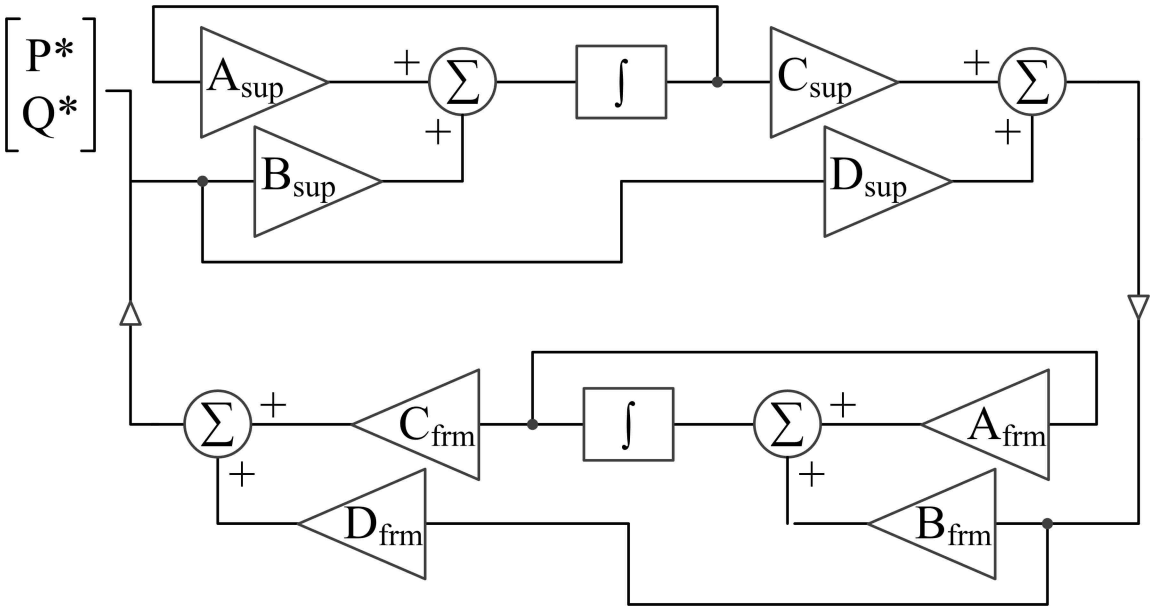

Figure 2.8 Grid-supporting and grid-forming model combination

derived as a single model, a new linearization point would need to be found for the full system each time an individual inverters parameters were changed. For n grid-supporting inverters and 1 grid-forming inverter, this would be system of $14n + 17$ nonlinear equations. As shown in Table 2.1, calculation times for these systems do not scale well and would quickly become prohibitively long. By contrast, the same system could be modeled as n independent grid-supporting units, and combined after linearization. With each parameter change, only a single 14 equation system would need to be solved.

Extending the model to include multiple grid-forming units does not provide the same benefit in terms of calculation time. In a system of multiple grid-forming units power is shared between inverters. Bus voltages and grid frequency must balance themselves in order to achieve equal power sharing. This process is highly nonlinear, and in order to model this behavior correctly a linearization point must be found for the equations of both grid-forming units. As long as the grid-forming units remain unchanged, though, any number of grid-supporting units may be connected to either inverter bus without requiring the linearization point to be recalculated.

Table 2.1 Nonlinear equation solver calculation times

PC	**System**	**ODE15s**	**ODE23s**	**ODE23t**	**ODE23tb**
A	Grid-Forming	0.304276	6.273586	0.328464	0.324085
	Grid-Supporting	0.320764	9.145176	0.332532	0.320739
	Combined	100.158032	127.772132	29.964732	0.651894
B	Grid-Forming	0.650037	15.704150	0.619770	0.551224
	Grid-Supporting	0.537896	12.900595	0.526117	0.528729
	Combined	165.194541	244.373168	0.918903	1.421644
C	Grid-Forming	1.427614	9.492107	0.611400	0.595118
	Grid-Supporting	0.515824	11.578296	0.533705	0.520852
	Combined	42.076199	95.284286	7.090146	0.795035

3. MODEL VERIFICATION AND ANALYSIS

The models of the grid-support unit acting in grid-tied operation and as part of an islanded microgrid are verified through a comparison of selected dynamic responses predicted by the models to those of a simulation, and also to those recorded in a hardware experiment. The dynamic responses include step changes in control inputs P^* and Q^*.

3.1. VERIFICATION METHODS

3.1.1. Simulation. Simulations of both grid-tied and grid-supporting operation were performed as part of the validation procedure. The simulations were done in MATLAB/Simulink with the PLECS blockset. Unmodeled aspects of the hardware implementation that are not modeled are included in the simulations. Specifically, the simulations include sampling and switching effects that are not included in either the linearized models or the nonlinear equations. The control systems are implemented in discrete time, and integration is approximated using the backward Euler method. This is consistent with the code programmed into the digital signal processors. Both the simulation and the hardware setup contain the same dead-time mitigation strategy, which is discussed in a later section.

3.1.2. Hardware Implementation. The hardware setup, like the simulation, consists of two inverters, local RL loads, and a grid connection. Each inverter and load can be connected to or withdrawn from the system independently. An autotransformer is used between the inverter outputs and the grid connection for the purpose of scaling the grid voltage down to a more manageable magnitude. The autotransformer was found to have some nonnegligible winding resistance and leakage inductance. These and other relevant component values of the hardware setup are shown in Table 3.1.

The inverters themselves are built around Infineon BSM30GP60 IGBT modules and controlled by Texas Instruments TMS320F28335 digital signal processors. Since the values of interest include transient responses of d- and q-axis quantities, it was necessary take this information from the digital signal processors, as opposed to

Table 3.1 Gains and physical parameters of hardware setup

Grid-Supporting Gains	
kp_P	0.01
ki_P	0.1
kp_Q	0.01
ki_Q	0.1
kp_{id}	1
ki_{id}	100
kp_{iq}	1
ki_{iq}	100
kp_{PLL}	0.25
ki_{PLL}	2

Grid-Forming Gains	
kp_f	0.1
ki_f	15
kp_v	0.1
ki_v	15
kp_{id}	5
ki_{id}	100
kp_{iq}	5
ki_{iq}	100
kp_{PLL}	0.25
ki_{PLL}	2

Hardware	
L_f	4.2 mH
r_f	0.3 Ω
L_c	0.5 mH
r_c	0.1 Ω
C_f	15 μF
R_d	2 Ω
L_{trafo}	0.1 mH
R_{trafo}	0.287 Ω
L_{load}	15 mH
R_{load}	12.5 Ω

measuring them externally. Due to the relatively large volume of data this generates and the limited storage space of the DSP, the data had to be transmitted in real time during the experiments and logged externally. The data was logged at 1 ms intervals. This was found to be the maximum possible rate at which the data could be exported without interrupting the inverter control code. In order to prevent this data rate limitation from affecting the results collected, control gains were designed such that the step change transients were slow enough to be fully observed. The gains used are shown in Table 3.1. The sampling period and full program cycle time is 100 μs, or 10 kHz. The switching frequency is 5 kHz, and duty ratios are updated every half switching period.

3.2. RESULTS

The model predictions are compared to results of simulation and hardware tests for step changes in P^* and Q^*. The grid-tied mode comparisons are shown first, followed by those for grid-supporting operation.

3.2.1. Grid-Tied Operation. The results of a P^* step change are shown in Figure 3.1. A command of 500 W is sent to the inverter at time t = 1.5 s. The dynamics shown include P_{avg}, Q_{avg}, ω_{PLL}, v_{od}, v_{oq}, i_{od}, and v_{oq} as subplots (a)

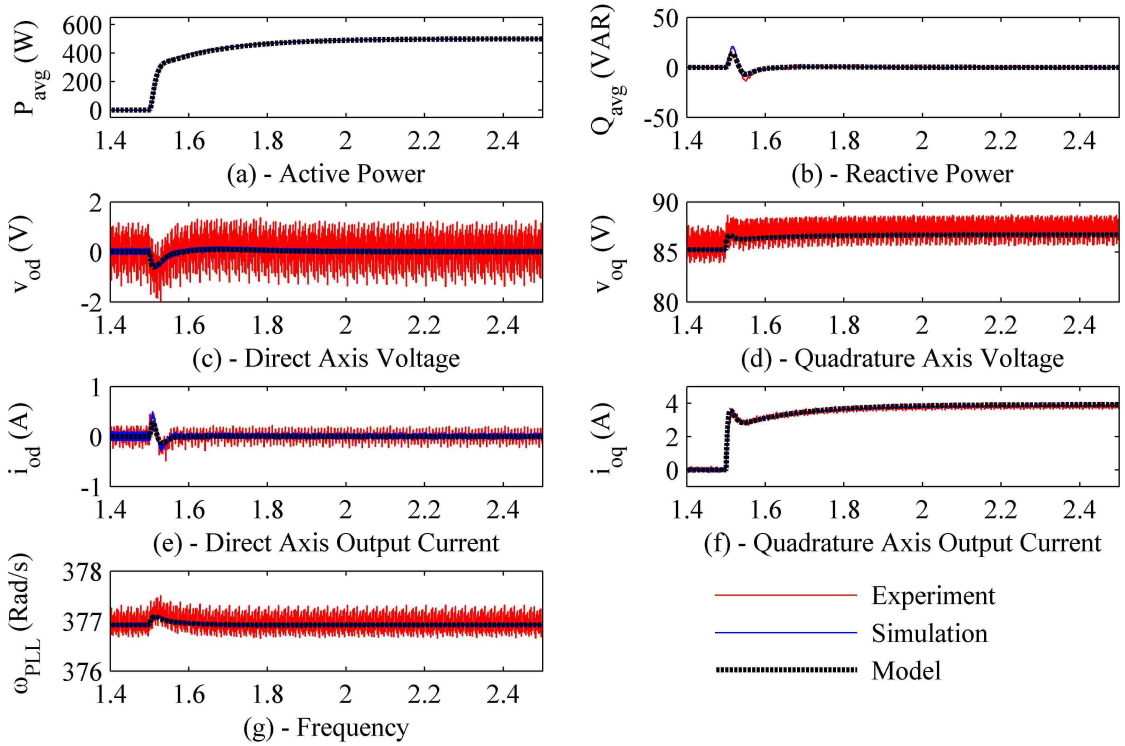

Figure 3.1 P^* step change in grid-tied operation

through (g), respectively. Experimental results are shown in red, simulation in blue, and model predictions as a dotted black line. The model predicts the response of all system states, but the integrator states are not shown because their values do not have physical significance. Filter currents i_{ld} and i_{lq} are also not shown due to their overall similarity to the output currents.

Similarly matching results are shown in Figure 3.2 for the Q^* step response. The most striking similarities in the model predictions for both control input changes are in the P_{avg} and Q_{avg} plots, in which the model predictions very nearly overlap the simulation and experimental results. These results display the model's ability to predict the behavior of a real grid-tied system.

3.2.2. Grid-Supporting Operation. The combined model predictions are shown for P^* and Q^* step changes in Figures 3.3 and 3.4, respectively. Figure 3.5 shows step changes in both control inputs simultaneously. The most visible difference between these plots and those of the grid-tied system is the switching noise in the simulation waveforms. While the grid source provided a continuous voltage in the

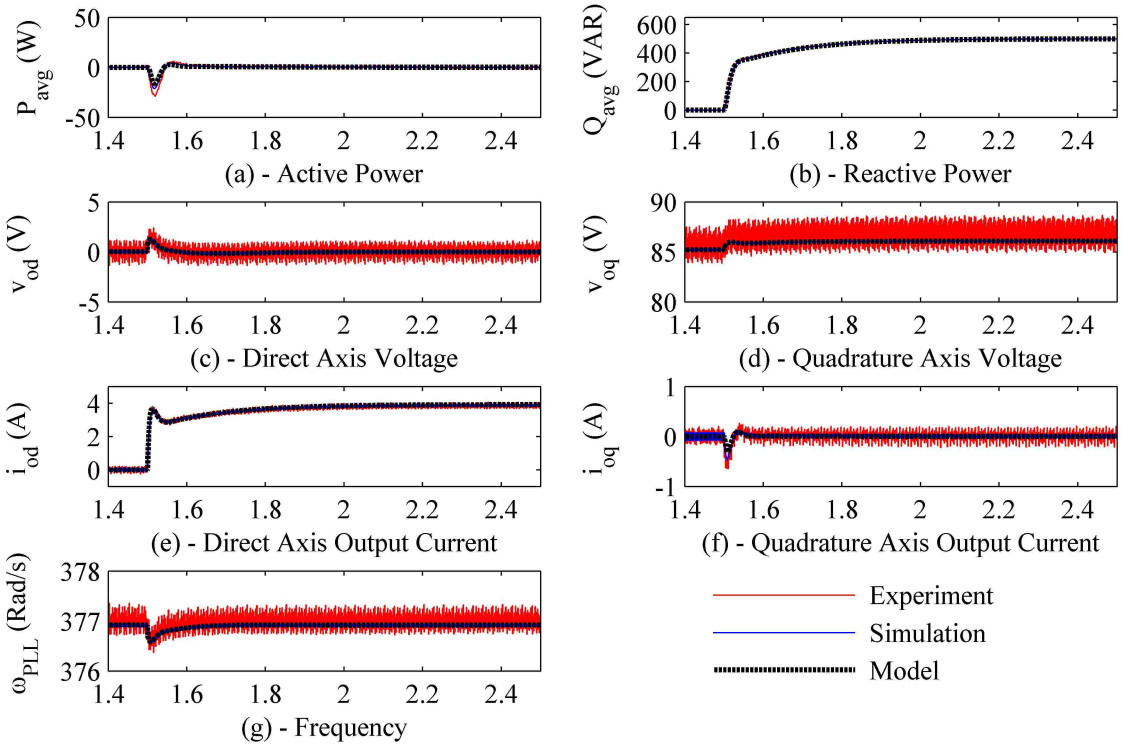

Figure 3.2 Q^* step change in grid-tied operation

grid-tied simulations, the voltage regulated by the grid-forming unit is subject to switching ripple, which is present at the grid-supporting unit's point of connection.

The most important aspect of the model is the ability to predict and describe P_{avg} and Q_{avg} transient responses. In this regard, the model is very successful. The dynamics of P_{avg} overlap the simulation and experimental results for the P^* step change, and the dynamics of Q_{avg} overlap for the P^* step change. There is some mismatch in the frequency and d-axis quantities for the P^* step change in Figure 3.3. The Q^* step response is much more accurate, though some small mismatch is present in the q-axis output current. The source of these errors is the presence of switching dead time in the simulation and experimental systems. Though an attempt was made to mitigate the dead time effects, the switching outputs do not (and cannot) perfectly match the averaged switch approximation used in the models.

Because of the nature of the dead time effects, which are discussed more thoroughly in Section 3.3, the d-axis quantities are more significantly impacted. In particular, the d-axis current is more difficult to control when close to zero. For this

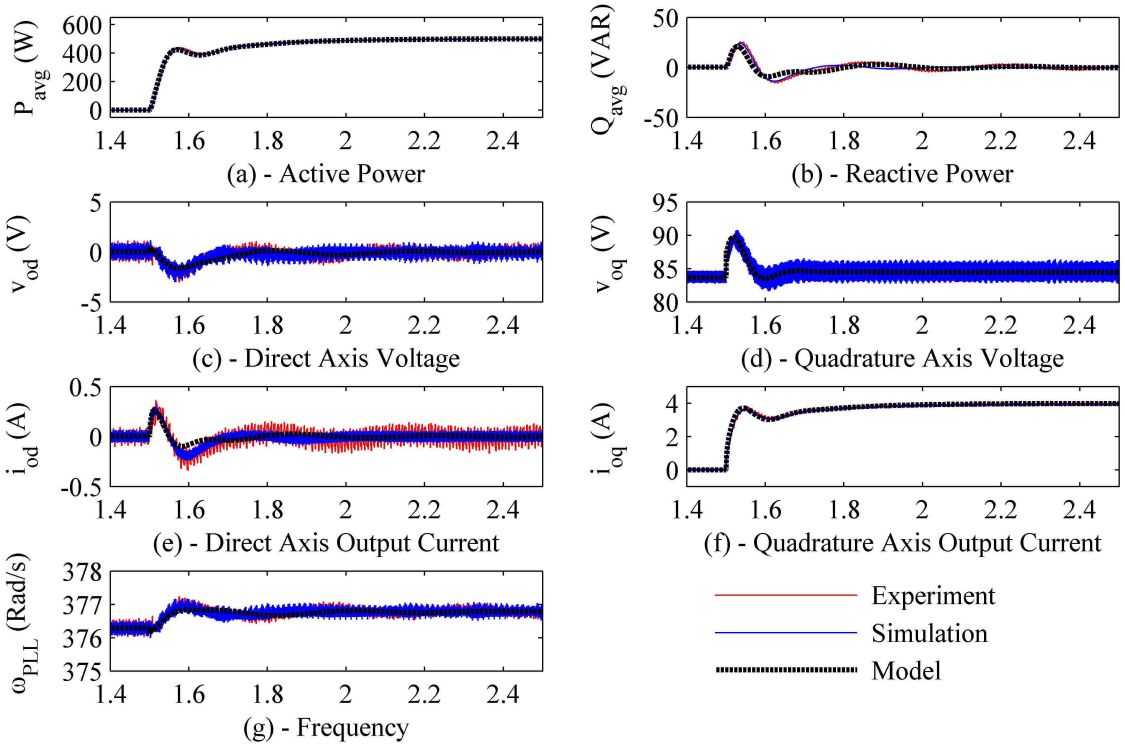

Figure 3.3 P^* step change in grid-supporting operation

reason, the dead time effects are most clearly visible in Figure 3.3, since Q is held at 0 VAR. When the d-axis is controlled to a specific value, as in Figures 3.4 and 3.5, the model dynamics more closely match the experimental results. In these cases the model is even more true to the experiment than the results of the simulation. The simulation includes the dead time mitigation strategy used by the DSP, but does not include all of the nonlinearities that necessitate the use of such a strategy. Specifically the on-resistance, rise and fall times, and saturation voltages of the IGBTs are not present in the simulation. Without these parameters the dead time mitigation strategy overcompensates for the simulated dead time effect.

The change in system damping between Figures 3.2 and 3.4 demonstrates the inadequacy of existing grid-tied inverter models in control design of grid-supporting inverters. In these responses, the gains of the controllers were selected using the model of the grid-tied system. When connected to a stiff grid, the system response is well damped. The response may not be perfect, but it is satisfactory. When connected to a microgrid the response becomes underdamped. The grid-supporting model may be

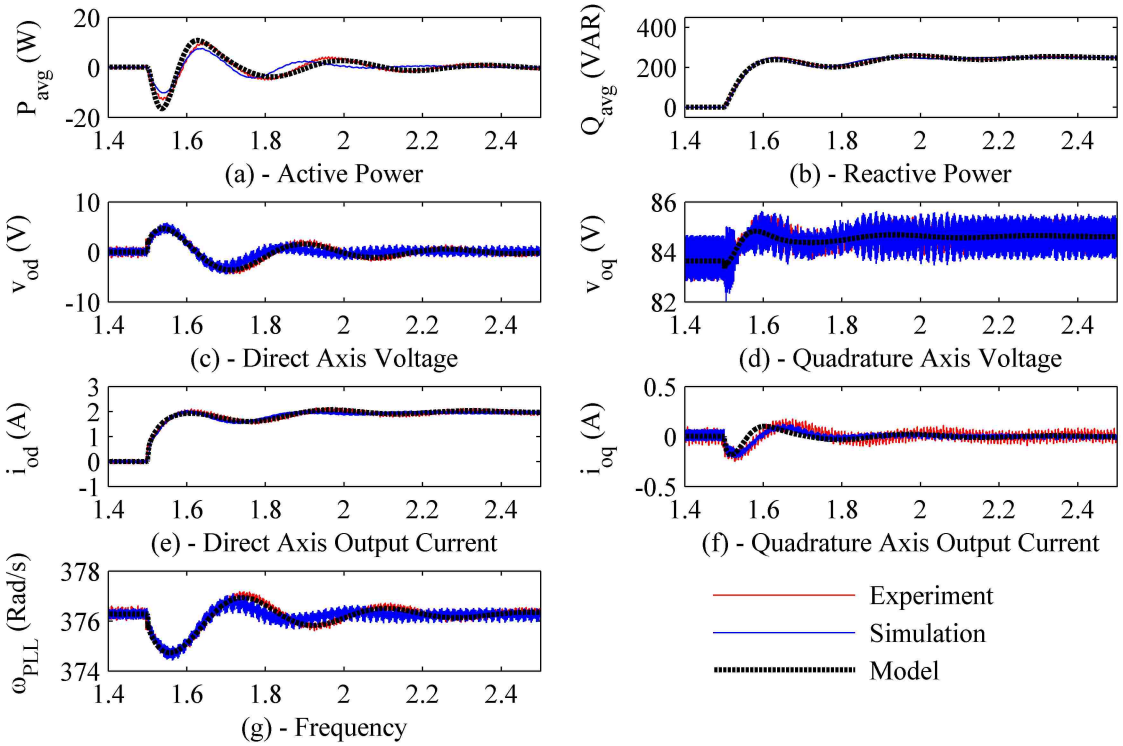

Figure 3.4 Q^* step change in grid-supporting operation

used to tune these gains and achieve a more desirable response. This is illustrated in Section 4, in which the response shown in Figure 3.4 is improved using the model combination process and established linear control methods.

3.3. IMPORTANCE OF MITIGATING EFFECTS OF DEAD TIME

Switching dead time, or time added to certain switching periods to prevent damaging shoot-through faults, was found to play a significant role in system dynamics. The inverter models are based on the average switch modeling technique, which approximates the output phase voltage as the average over a single switching period. This approximation ignores the presence of dead time, which is a necessity in practical application, and as a result the models' performances are limited. In order to maintain accuracy, either the models must be adjusted to account for the effects of dead time or the modulation strategy used to drive the switches must be altered to preemptively mitigate the effects of dead time. Given the complex nonlinearity of the dead time effects and the availability of simple modulation strategy modifications

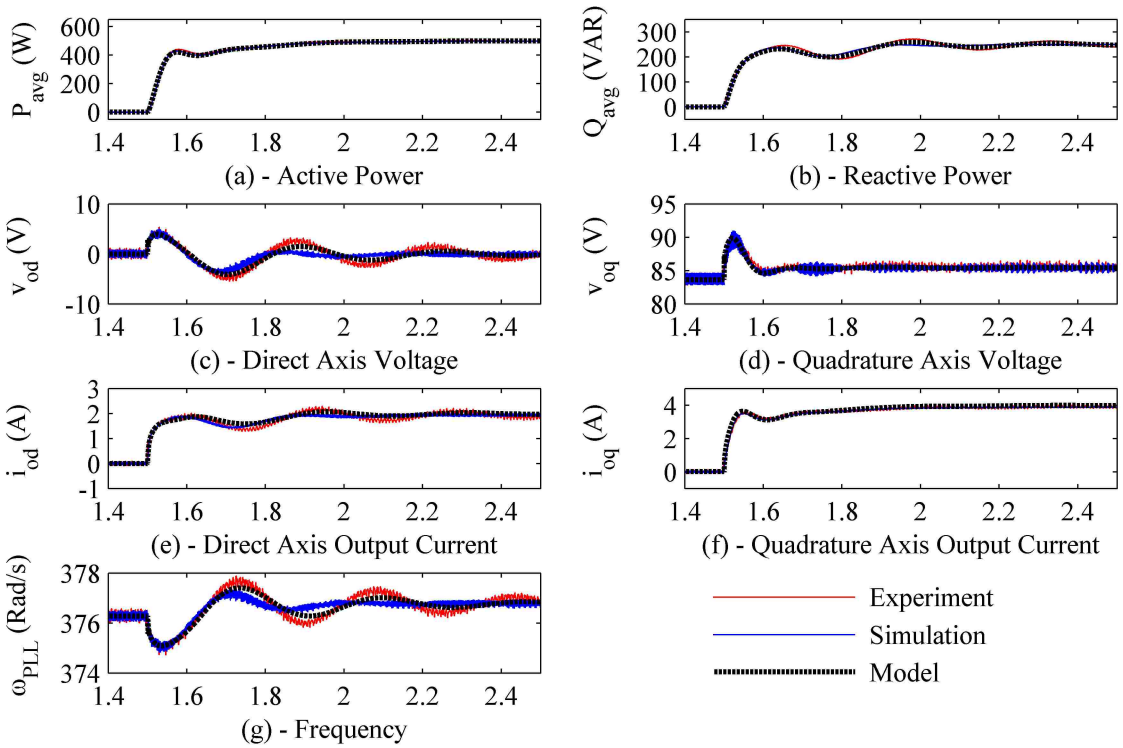

Figure 3.5 P^* and Q^* step change in grid-supporting operation

in literature, the latter option was chosen for this work. Without the dead time mitigation strategy, the dynamics observed in simulation and hardware experiments are significantly different than the model predictions.

3.3.1. Effect on Model Performance. The clearest evidence of the effect of dead time is found in Figure 3.3, the dynamic response of a step change in P^*. The manner in which the d-axis is affected makes the dead time more problematic to the quantities controlled on the d-axis. In order to quantify the impact of dead time in a synchronous reference frame, the outputs of the SVPWM must be examined in more detail.

In [8], equations describing the effects of inserted dead time, transistor rise and fall times, and saturation voltages on output phase voltages are presented for a three phase inverter using SVPWM. These equations, considering only the dead time effect, are as follows:

$$V_{max}^{+} = \left(\frac{T_1}{T_S}\right)\left(\frac{2}{3}V_{DC}\right) + \left(\frac{T_2}{T_S}\right)\left(\frac{1}{3}V_{DC}\right) - \left(\frac{T_d}{T_S}\right)\left(\frac{1}{3}V_{DC}\right) \tag{53}$$

$$V_{max}^{-} = \left(\frac{T_1}{T_S}\right)\left(\frac{2}{3}V_{DC}\right) + \left(\frac{T_2}{T_S}\right)\left(\frac{1}{3}V_{DC}\right) - \left(\frac{T_d}{T_S}\right)\left(\frac{2}{3}V_{DC}\right) \tag{54}$$

$$V_{mid}^{+} = \left(\frac{T_1}{T_S}\right)\left(\frac{-1}{3}V_{DC}\right) + \left(\frac{T_2}{T_S}\right)\left(\frac{1}{3}V_{DC}\right) - \left(\frac{T_d}{T_S}\right)\left(\frac{1}{3}V_{DC}\right) \tag{55}$$

$$V_{mid}^{-} = \left(\frac{T_1}{T_S}\right)\left(\frac{-1}{3}V_{DC}\right) + \left(\frac{T_2}{T_S}\right)\left(\frac{1}{3}V_{DC}\right) + \left(\frac{T_d}{T_S}\right)\left(\frac{1}{3}V_{DC}\right) \tag{56}$$

$$V_{min}^{+} = \left(\frac{T_1}{T_S}\right)\left(\frac{-1}{3}V_{DC}\right) + \left(\frac{T_2}{T_S}\right)\left(\frac{-2}{3}V_{DC}\right) + \left(\frac{T_d}{T_S}\right)\left(\frac{2}{3}V_{DC}\right) \tag{57}$$

$$V_{min}^{-} = \left(\frac{T_1}{T_S}\right)\left(\frac{2}{3}V_{DC}\right) + \left(\frac{T_2}{T_S}\right)\left(\frac{1}{3}V_{DC}\right) + \left(\frac{T_d}{T_S}\right)\left(\frac{1}{3}V_{DC}\right) \tag{58}$$

$$V_{max} = \begin{cases} V_{max}^{+} & : V_{mid}^{*} \geq 0 \\ V_{max}^{-} & : V_{mid}^{*} < 0 \end{cases} \tag{59}$$

$$V_{mid} = \begin{cases} V_{mid}^{+} & : V_{mid}^{*} \geq 0 \\ V_{mid}^{-} & : V_{mid}^{*} < 0 \end{cases} \tag{60}$$

$$V_{min} = \begin{cases} V_{min}^{+} & : V_{mid}^{*} \geq 0 \\ V_{min}^{-} & : V_{mid}^{*} < 0 \end{cases} \tag{61}$$

Variables T_1, T_2, and T_0 are the switching vector times of the SVPWM, which are calculated from the commanded voltages V_{abc}^{*}, switching period T_S, and DC link voltage V_{DC}:

$$T_1 = \left(\frac{2V_{max}^{*} + V_{min}^{*}}{V_{DC}}\right)T_S \tag{62}$$

$$T_2 = \left(\frac{V_{max}^{*} + 2V_{min}^{*}}{V_{DC}}\right)T_S \tag{63}$$

$$T_0 = T_S - T_1 - T_2 \tag{64}$$

Values of V_{max}^{*}, V_{mid}^{*}, and V_{min}^{*} may each be either V_a^{*}, V_b^{*}, or V_c^{*} depending on the switching vector angle. For a balanced three phase voltage, where switching vector angle θ_{ref} is equal to the phase angle of V_a^{*}, the max, min, and middle voltages for each phase are given in Table 3.2.

The full conversion between commanded voltages V_{abc}^{*} and actual voltages V_{abc} can be achieved by first determining the appropriate voltages V_{max}^{*}, V_{mid}^{*}, and V_{min}^{*} from Table 3.2, substituting these values into Equations (62), (63), and (64), and

finally selecting from the appropriate output voltage equations for V_{abc} according to Table 3.3. This results in a discontinuous three phase voltage waveform. This is shown graphically in Figure 3.6 for a balanced commanded voltage with an amplitude of 1 V, frequency of 60 Hz, DC link voltage of $\sqrt{3}$ V, and switching frequency 6 kHz. Subplot (a) shows the varying effect of different dead times in the stationary reference frame. The effect is subtle enough that it is only barely noticeable at this scale. Subplots (b) and (c) show the same waveforms transformed into synchronous reference frame as d-axis and q-axis voltages, respectively. These plots much more clearly show the distortions caused by the dead time.

The disturbance in the q-axis voltage has little variation over the full waveform period but decreases the magnitude of the output. This type of disturbance can be counteracted easily by the current controllers, whose integral components can ensure

Table 3.2 Max, mid, and min voltages by switching vector angle

$\boldsymbol{\theta_{ref}}$	$(\mathbf{0}, \frac{\boldsymbol{\pi}}{\mathbf{3}}]$	$(\frac{\boldsymbol{\pi}}{\mathbf{3}}, \frac{\mathbf{2}\boldsymbol{\pi}}{\mathbf{3}}]$	$(\frac{\mathbf{2}\boldsymbol{\pi}}{\mathbf{3}}, \boldsymbol{\pi}]$	$(\boldsymbol{\pi}, \frac{\mathbf{4}\boldsymbol{\pi}}{\mathbf{3}}]$	$(\frac{\mathbf{4}\boldsymbol{\pi}}{\mathbf{3}}, \frac{\mathbf{5}\boldsymbol{\pi}}{\mathbf{3}}]$	$(\frac{\mathbf{5}\boldsymbol{\pi}}{\mathbf{3}}, \mathbf{2}\boldsymbol{\pi}]$
V^*_{max}	V^*_a	V^*_b	V^*_b	V^*_c	V^*_c	V^*_a
V^*_{mid}	V^*_b	V^*_a	V^*_c	V^*_b	V^*_a	V^*_c
V^*_{min}	V^*_c	V^*_c	V^*_a	V^*_a	V^*_b	V^*_b

Table 3.3 Output phase voltages by switching vector angle

$\boldsymbol{\theta_{ref}}$	$(\mathbf{0}, \frac{\boldsymbol{\pi}}{\mathbf{6}}]$	$(\frac{\boldsymbol{\pi}}{\mathbf{6}}, \frac{\boldsymbol{\pi}}{\mathbf{3}}]$	$(\frac{\boldsymbol{\pi}}{\mathbf{3}}, \frac{\boldsymbol{\pi}}{\mathbf{2}}]$	$(\frac{\boldsymbol{\pi}}{\mathbf{2}}, \frac{\mathbf{2}\boldsymbol{\pi}}{\mathbf{3}}]$	$(\frac{\mathbf{2}\boldsymbol{\pi}}{\mathbf{3}}, \frac{\mathbf{5}\boldsymbol{\pi}}{\mathbf{6}}]$	$(\frac{\mathbf{5}\boldsymbol{\pi}}{\mathbf{6}}, \boldsymbol{\pi}]$
V_a	V^-_{max}	V^+_{max}	V^+_{mid}	V^-_{mid}	V^-_{mid}	V^+_{mid}
V_b	V^-_{mid}	V^+_{mid}	V^+_{max}	V^-_{max}	V^-_{max}	V^+_{max}
V_c	V^-_{min}	V^+_{min}	V^+_{min}	V^-_{min}	V^-_{mid}	V^+_{mid}

$\boldsymbol{\theta_{ref}}$	$(\boldsymbol{\pi}, \frac{\mathbf{7}\boldsymbol{\pi}}{\mathbf{6}}]$	$(\frac{\mathbf{7}\boldsymbol{\pi}}{\mathbf{6}}, \frac{\mathbf{4}\boldsymbol{\pi}}{\mathbf{3}}]$	$(\frac{\mathbf{4}\boldsymbol{\pi}}{\mathbf{3}}, \frac{\mathbf{3}\boldsymbol{\pi}}{\mathbf{2}}]$	$(\frac{\mathbf{3}\boldsymbol{\pi}}{\mathbf{2}}, \frac{\mathbf{5}\boldsymbol{\pi}}{\mathbf{3}}]$	$(\frac{\mathbf{5}\boldsymbol{\pi}}{\mathbf{3}}, \frac{\mathbf{11}\boldsymbol{\pi}}{\mathbf{6}}]$	$(\frac{\mathbf{11}\boldsymbol{\pi}}{\mathbf{6}}, \mathbf{2}\boldsymbol{\pi}]$
V_a	V^+_{min}	V^-_{min}	V^-_{mid}	V^+_{mid}	V^-_{max}	V^+_{max}
V_b	V^+_{mid}	V^-_{mid}	V^-_{min}	V^+_{min}	V^+_{min}	V^-_{min}
V_c	V^+_{max}	V^-_{max}	V^-_{max}	V^+_{max}	V^+_{mid}	V^-_{mid}

that the necessary voltage magnitude is supplied. The disturbance on the d-axis, however, is more problematic from a control perspective. As part of the PLL, the d-axis voltage is controlled to 0. This variation above and below 0 V causes slight oscillations in the calculated frequency and phase angle and, consequently, impacts the dynamics of the d-axis quantities. This effect is most severe when i_{ld} is small, because the small errors in d-axis current resulting from the voltage variations dominate the output of the d-axis current controller. When a significant current is commanded on the d-axis, as in the case of a Q^* step change, these errors become small compared to the value of the integrator state, minimizing their negative effects.

3.3.2. Dead Time Effect Mitigation Strategy. In order to minimize the effects of dead time, the strategy proposed in [8] is adopted. This tactic involves preemptively modifying switching intervals in the SVPWM to account for time spent in unintended modes of conduction. Since complementary gates do not switch simultaneously, the conduction paths during the dead time between switching are forced through the antiparallel diodes. Time spent in these conduction modes decreases the

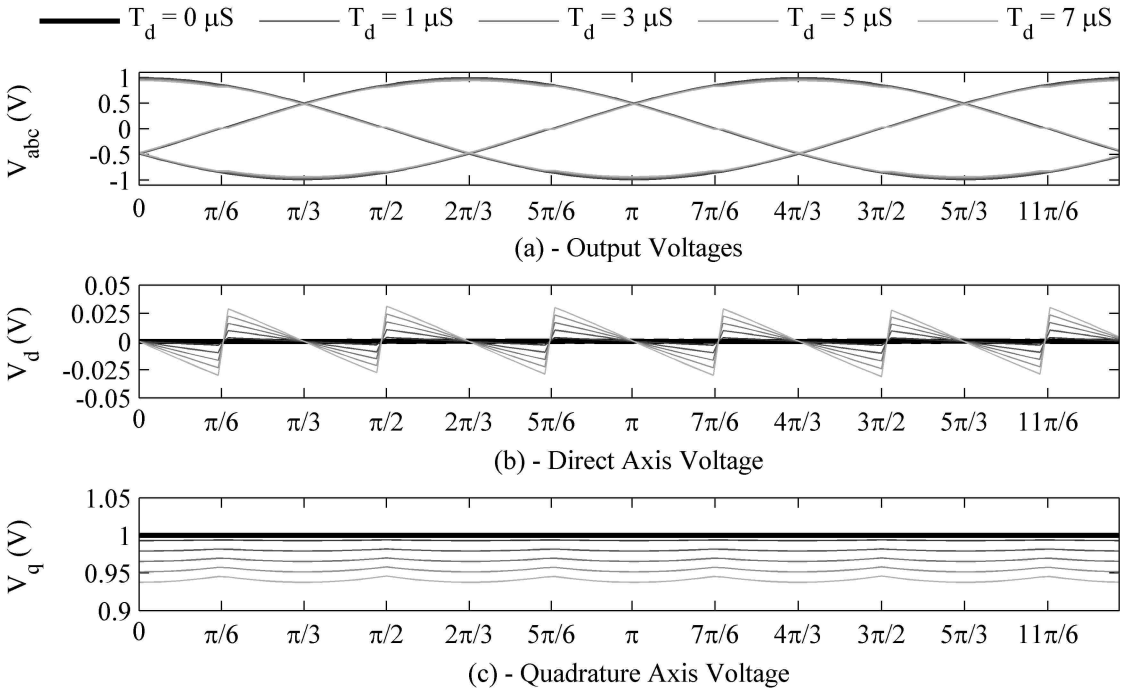

Figure 3.6 Effects of dead time in synchronous reference frame

active time of one of the switching vectors, depending on the polarity of the middle phase current. By inserting this time into the affected vector period, the effect of dead time can be limited. This is done as follows:

$$T_1 = \begin{cases} \left(\frac{2V^*_{max}+V^*_{min}}{V_{DC}}\right)T_S & : i_{l,mid} \geq 0 \\ \left(\frac{2V^*_{max}+V^*_{min}}{V_{DC}}\right)T_S + T_d & : i_{l,mid} < 0 \end{cases} \tag{65}$$

$$T_2 = \begin{cases} \left(\frac{V^*_{max}+2V^*_{min}}{V_{DC}}\right)T_S + T_d & : i_{l,mid} \geq 0 \\ \left(\frac{V^*_{max}+2V^*_{min}}{V_{DC}}\right)T_S & : i_{l,mid} < 0 \end{cases} \tag{66}$$

The current $i_{l,mid}$ in equations (65) and (66) is subject to the same phase arrangement as the voltages given in Table 3.2. These equations are simplified versions of those proposed in [8], which include rise and fall times and voltage drops across the IGBTs.

4. EIGENVALUE ANALYSIS AND SYSTEM DESIGN

The intended application of the small-signal model discussed in the previous chapters is as an analysis and design tool for grid-supporting inverters in microgrid systems. An eigenvalue analysis of the two inverter system allows problematic modes of oscillation to be identified and provides valuable insights into the interactions of the inverter control systems, which is otherwise unavailable. Stability issues may be remedied through an assessment of the changes in eigenvalue loci with variations in system parameters such as control gains or filter hardware values. A process of iterative linearizations with incremental parameter changes allows relationships between eigenvalue positions and the selected parameters to be determined. These relationships, while general, allow informed decisions to be made in terms of the selection of hardware components and tuning of controller gains. As an example of this process, the relationships observed in the eigenvalue analysis are used to determine new controller gains for the grid-supporting inverter that significantly improve the damping in the system response.

The models provide detailed information on both the grid-supporting and grid-forming inverters. Since the focus here is on the design of grid-supporting inverters for use in microgrids, only the design considerations of the grid-supporting unit will be discussed. A white-box approach is taken with respect to the grid-forming unit: its internal parameters are known, but may not be changed. The purpose of this is to simulate a situation in which a grid-supporting inverter is designed for use in an existing microgrid system composed of other inverters. These existing inverters are assumed to have been designed with different objectives in mind. The new inverter should be designed in such a way that it does not negatively affect the stability of the existing system. The design process should also not require the control gains or filter components of the previously existing inverter to be altered. However, knowledge of the internal parameters of the grid-forming unit provides useful insights into the behavior of the combined system, so it is assumed that the system designer has access to this information in the following discussions. A secondary reason for the white-box treatment of the grid-forming inverter is to limit the scope of this work. A full

discussion of the design considerations for a system of multiple grid-forming units is both beyond the limits of what could be adequately covered here and beyond the capabilities of this linearized model.

4.1. SYSTEM ANALYSIS

The eigenvalues of the system when linearized around the operating point found for the gains and component values in Table 3.1 are shown in Figure 4.1. The same eigenvalues are listed in Table 4.1 as well. The pair furthest to the left on the complex plane are related to the resistance of the virtual resistor r_n and have no physical significance. The rest of the eigenvalues can be separated into two groups based on proximity to the imaginary axis. The first group is arbitrarily defined to include all eigenvalues $\lambda_i = \sigma_i + j\omega_i$ for which $\sigma_i < -100\ s^{-1}$, or in other words all eigenvalues clearly visible in Figure 4.1. The second group includes those clustered close to the origin.

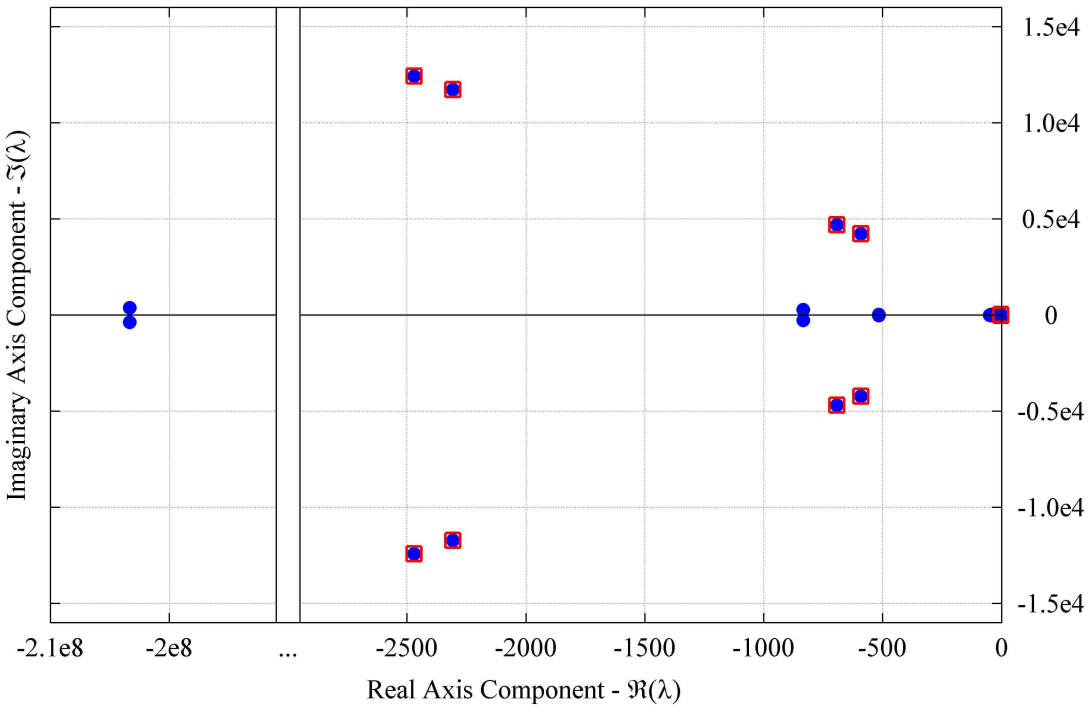

Figure 4.1 Eigenvalue locations on complex plane

Table 4.1 System eigenvalues

$\Re(\lambda)$	$\Im(\lambda)$	Damping Ratio	Natural Frequency	Mode Index
-2.03×10^8	± 376.29	100	3.24×10^7	1, 2
-2.4703×10^3	$\pm 1.2419 \times 10^4$	19.51	2.0152×10^3	3, 4
-2.3073×10^3	$\pm 1.1718 \times 10^4$	19.32	1.9008×10^3	5, 6
-7.9545×10^3	0	100	1.2660×10^3	N/A
-692.85	$\pm 4.6894 \times 10^3$	14.62	754.44	7, 8
-591.91	$\pm 4.2252 \times 10^3$	13.87	679.03	9, 10
-834.76	± 281.6	94.76	140.21	11, 12
-516.52	± 20.963	99.92	82.274	13, 14
-21.972	± 37.935	50.12	6.9772	15, 16
-45.296	± 24.554	87.91	8.2002	17, 18
-49.725	0	100	7.9140	N/A
-50.248	0	100	7.9972	N/A
-35.403	± 9.795	96.38	5.8462	19, 20
-3.040	± 17.249	17.36	2.7875	21, 22
-10.589	± 7.576	81.33	2.0722	23, 24
-6.205	± 0.926	98.40	0.9985	25, 26
-5.794	0	100	0.9222	N/A
0	0	100	0	N/A

Each of these groups contains both well-damped and eigenvalues and potentially problematic eigenvalues. In this context, all eigenvalues with damping ratios less than 30% are considered problematic. Without being quickly damped, these oscillations may significantly affect the performance of the system. The physical consequences of oscillations in controlled values may include loss of efficiency, increased wear and tear on equipment, and, in severe cases, control system instability. Oscillations in output voltage and current may negatively affect the harmonic content of the microgrid and the quality of power supplied to the loads. Oscillations in voltage are particularly disruptive because of their effect on the inverters' calculated phase angles through the PLL. In addition to the damping ratio, the frequency of oscillation must be considered. Some frequencies may be more problematic than others. Harmonics of

the nominal grid frequency are of particular interest. Table 4.1 shows the real and imaginary components of all eigenvalues, their corresponding damping ratios and natural frequencies, and an assigned mode index, which will be used to refer back to problem modes later. The eigenvalue rows with less than satisfactory damping ratios are given in red text.

To determine general relationships between problem modes and the states of the system, a participation matrix is calculated following the procedure in [7]. The participation matrix is composed of dimensionless values corresponding to the relative participation of a given state variable in a given mode, or participation factors. A higher participation factor indicates that a state is more active than others in a system mode. Considering participation factors less than 0.05 as negligible and plotting those remaining results in the chart shown in Figure 4.2. Again, only the states of the grid-supporting system are considered. States of the grid-forming inverter may strongly

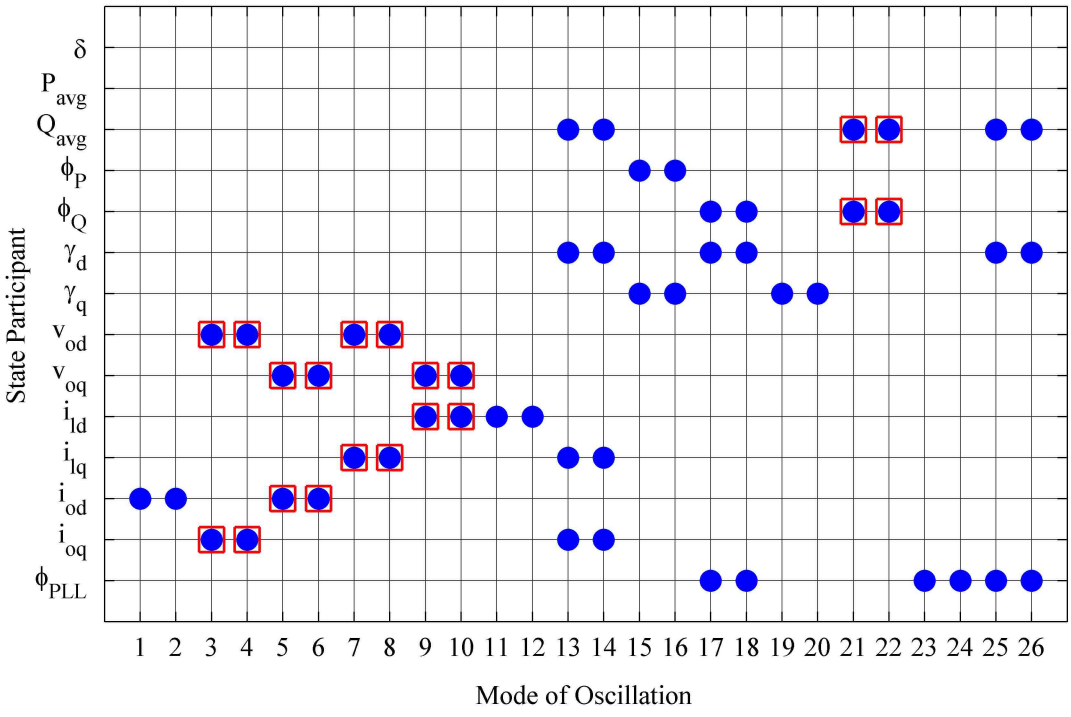

Figure 4.2 Chart of states participating in system modes

participate in problem modes, but here can only be damped through changes in grid-supporting inverter parameters. Red boxes are used in the participation factor chart to indicate the problem modes identified in Table 4.1.

4.1.1. Fast Group Eigenvalues. The faster group contains two sets of eigenvalue pairs that are of interest. The first set is made up of those corresponding to modes 3, 4, 5, and 6. The natural frequencies of this set are at 2.015 kHz and 1.901 kHz. The second set, including modes 7, 8, 9, and 10, have natural frequencies at 754.44 and 679.03 Hz. Using the values of L_f, C_f, and L_C in Table 3.1, the resonant frequency of the LCL filter is 1.944 kHz. Additionally, when considering the 15 mH load inductance contained in the grid-forming inverter system, the resonant frequency of the grid-forming unit's filter and load is 714.85 Hz. The calculations of resonant frequencies here are performed using the following equation from [9], where L_T includes both coupling and load inductance:

$$f_{res} = \frac{1}{2\pi}\sqrt{\frac{L_f + L_T}{L_f C_f L_T}} \tag{67}$$

The similarity of the resonant frequencies to the natural frequency of these underdamped modes indicates that modes 3, 4, 5, and 6 are strongly related to the inverters' LCL filters and modes 7, 8, 9, and 10 to the filters and load. Initially it may appear that each inverter contributes one eigenvalue pair to each of these sets, but observing the systems' eigenvalues before and after the models are combined shows that this is not the case. Modes 3, 4, 5, and 6 in the combined system are very nearly unchanged from their positions in the grid-supporting system alone, and the same is true of modes 7, 8, 9, and 10 in the grid-forming system. This is shown in Figure 4.3.

Unfortunately, because modes 7, 8, 9, and 10 in the combined system seem to be at least primarily dependent on parameters in the domain of the grid-forming inverter, it may be difficult to design the grid-supporting inverter in a way that significantly improves the damping ratios of these modes. However, the participation factor chart in Figure 4.2 shows that states of the grid-supporting system do participate in these modes in some capacity. The participation factor reveals other interesting relationships as well. Both sets of eigenvalues are participated in by v_{odq}, but modes 3, 4, 5,

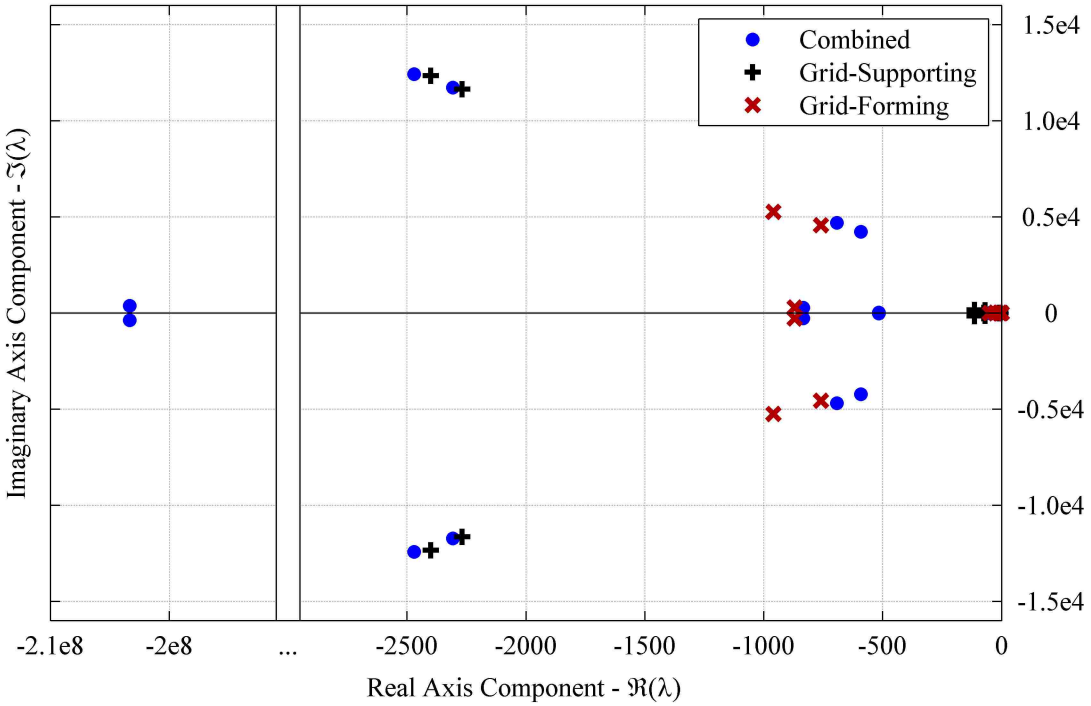

Figure 4.3 Eigenvalues inherited from individual inverter models

and 6 are more closely related to i_{odq}, while modes 7, 8, 9, and 10 are related to i_{ldq}. Since v_{odq} is regulated by the grid-forming inverter, not the grid-supporting inverter, only the control of the currents may be influenced. Moreover, the filter and output currents are controlled in different loops of the control system, and the d-axis and q-axis quantities each have their own controller. This one-to-one pairing of eigenvalues and controlled currents suggests that it may be possible to independently control the position of each eigenvalue pair with changes to a corresponding controller.

4.1.2. Slow Group Eigenvalues. The eigenvalues nearest to the imaginary axis are shown in Figure 4.4. These are the eigenvalues shown clustered around the origin in Figure 4.1. Figure 4.5 shows the eigenvalue positions at this scale before and after model combination. These eigenvalues are related to interactions between the inverter controllers, and change more significantly during the combination process than those related to the output filters. There is only one pair of problem modes much less damped than the others: modes 21 and 22. The natural frequency is slow enough

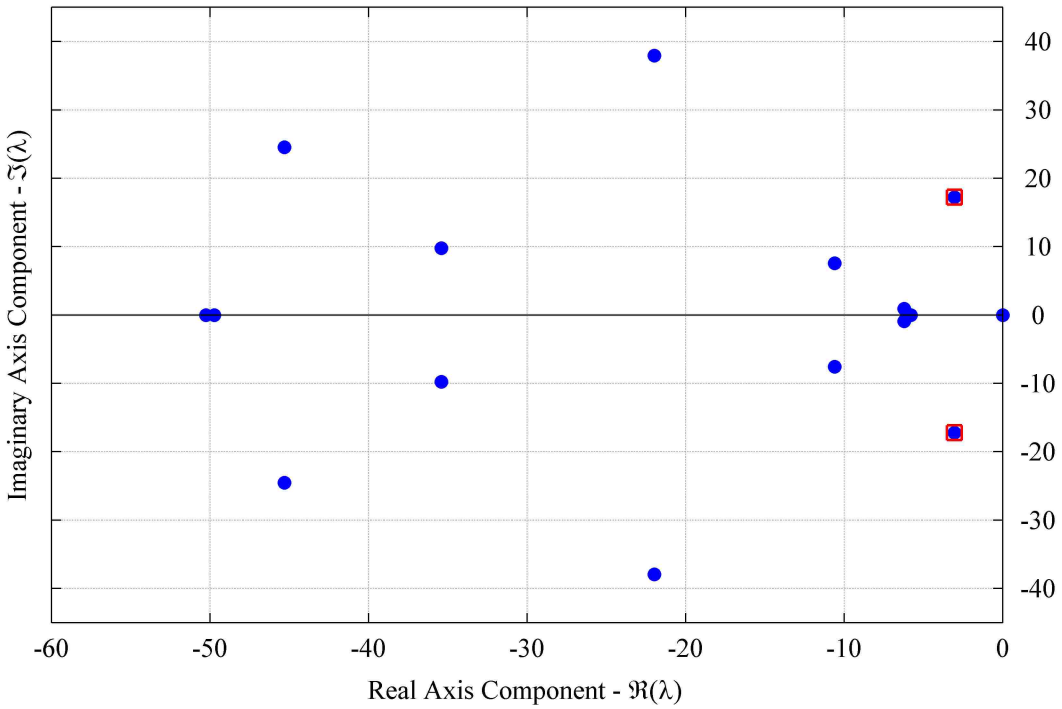

Figure 4.4 Inset of slowest eigenvalues

that the oscillation is visible in the plots of the Q^* step response in the experimental results. This can be seen in Figures 3.4 and 3.5 in the preceding section.

The participation factor chart shows that this mode is most related to Q_{avg} and the Q controller state, ϕ_Q. This may indicate a lack of damping in the outermost control loop. However, because reactive power is controlled through the d-axis current, controllers in both loops should be considered suspect. If the Q controller is designed in such a way that the changes in i^*_{ld} passed to the d-axis controller are faster than its gains allow it to react, the change in design will provide no benefit. The gains of both controllers will need to be matched appropriately.

This low frequency underdamped response occurs only in grid-supporting operation, though the same set of gains results in a well-damped response in grid-tied operation. This means that a well-designed grid-tied inverter may still experience issues caused by this mode when connected to a microgrid system. In contrast to the higher frequency issues related to the LCL filters, this underdamped response cannot be addressed using individual inverter models, and necessitates a more comprehensive

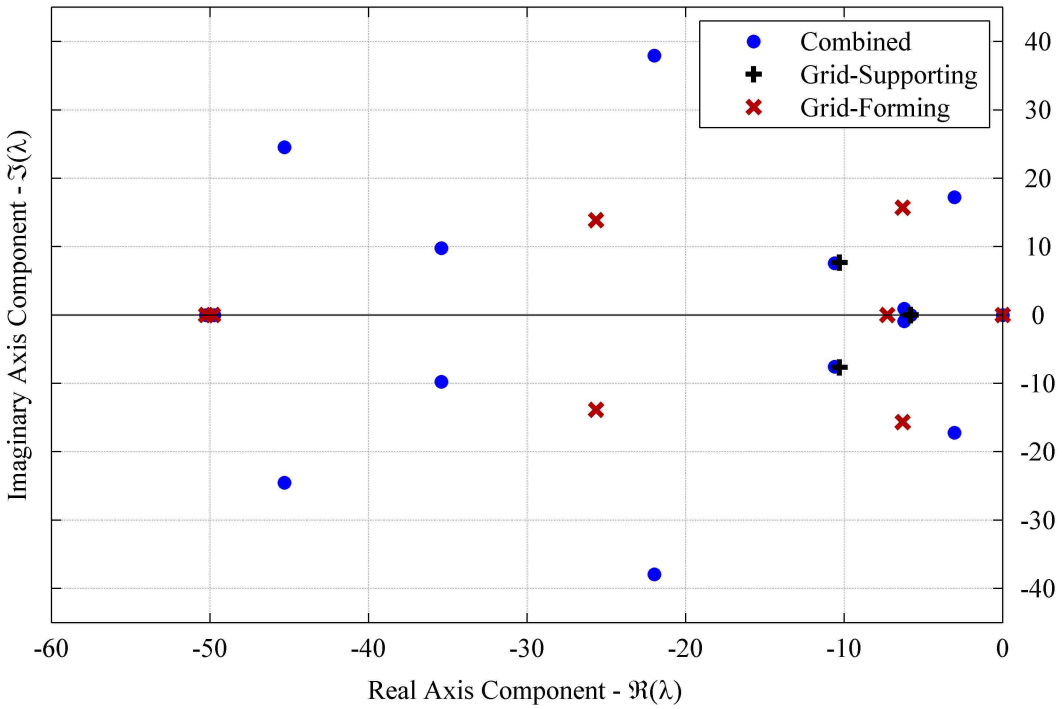

Figure 4.5 Inset of eigenvalues inherited from individual inverter models

view of the system. The model combination process and resulting combined system model provide a way for the system designer to identify and remedy these issues. This is the focus of Section 4.2.

4.2. DESIGN APPLICATIONS

Using the information gained from the parameter-eigenvalue relationships presented in the preceding section, informed decisions may be made on how controllers or filters should be designed to achieve better damping and stability.

4.2.1. Filter Design. Two sets of poorly damped eigenvalues are related to the filters used to connect the inverters to the microgrid. It is possible that the damping of these modes may be increased through changes in the hardware components used to construct the filters. The simplest method of increasing damping is to increase the resistance of R_d, since its sole purpose is to provide damping. However, this decreases the overall efficiency of the converter. Another solution is to replace

the current control loop with a more complex active damping controller. If possible, though, it is desirable to increase the damping without decreasing efficiency or redesigning the control system.

The primary free variables in terms of filter design are L_f and C_f. L_C may also be manipulated, but in many cases this parameter is set by an isolating transformer or line impedance. The range over which L_f and C_f are allowed to vary must be limited by the original goals of filter design. A full step-by-step LCL design procedure is given in [9]. The procedure includes frequency constraints to limit resonance, recommending that the resonant frequency of the filter be between 10 times the line frequency and half the switching frequency. This procedure was used in the initial design of the grid-supporting inverter, and its constraints should still be observed in the new design.

By iteratively changing the values of L_f and C_f in the model and plotting the corresponding eigenvalues, the relative change in eigenvalue location with filter inductance and capacitance changes may be observed. In Figure 4.6, the movement of the poorly damped eigenvalues is shown. Subplot (a) shows the full range of movement, while subplots (b) and (c) show zoomed in views of the two sets. Since there is considerable overlap between the movement of adjacent eigenvalues 3 and 5 (or 4 and 6), they are plotted independently in subplot (b) for clarity. The plot shows both changes in L_f and C_f. Each successive value of L_f is brighter than the last, increasing from 2 mH to 5 mH in increments of 0.3 mH. Values of C_f increase in increments of 1 μF from 2 μF, denoted by a square marker, to 25 μF, denoted by a circle.

As expected, the imaginary component and natural frequency of these eigenvalues changes significantly with filter component changes. The plot also shows that by selecting larger capacitance values it is possible to increase the damping in the system without requiring an increase in damping resistance. In Figure 4.7, the damping ratio values are plotted against component value changes. It is clear in this plot that the increases in capacitance for a given inductance value increase the damping ratio of the problem modes. However, while C_f is increased linearly, the increases in damping ratio begin to taper off for the least damped of the modes. Increasing the capacitance beyond the range of this plot will provide diminished returns on system damping,

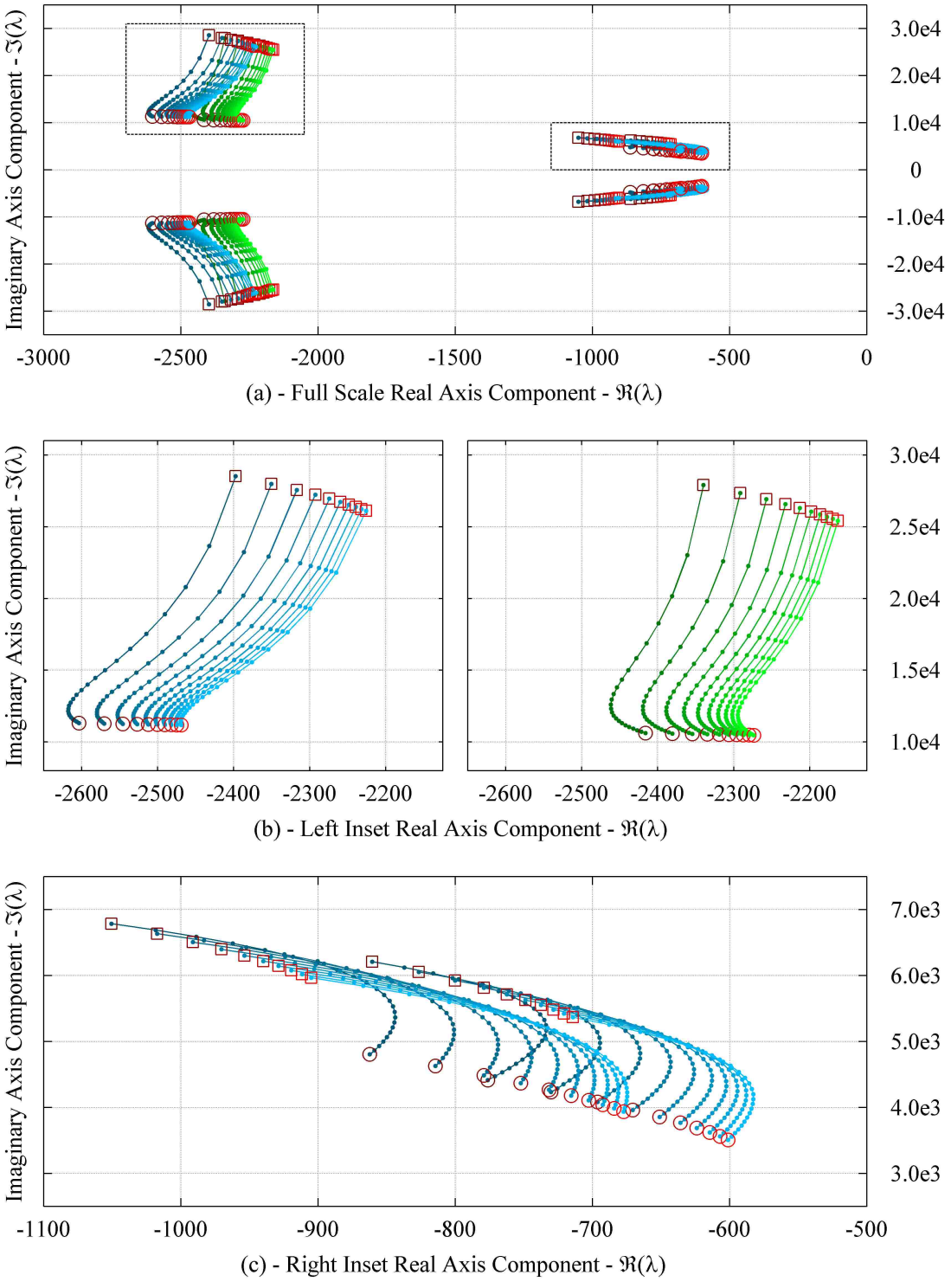

Figure 4.6 Eigenvalue position movement with increases in L_f and C_f

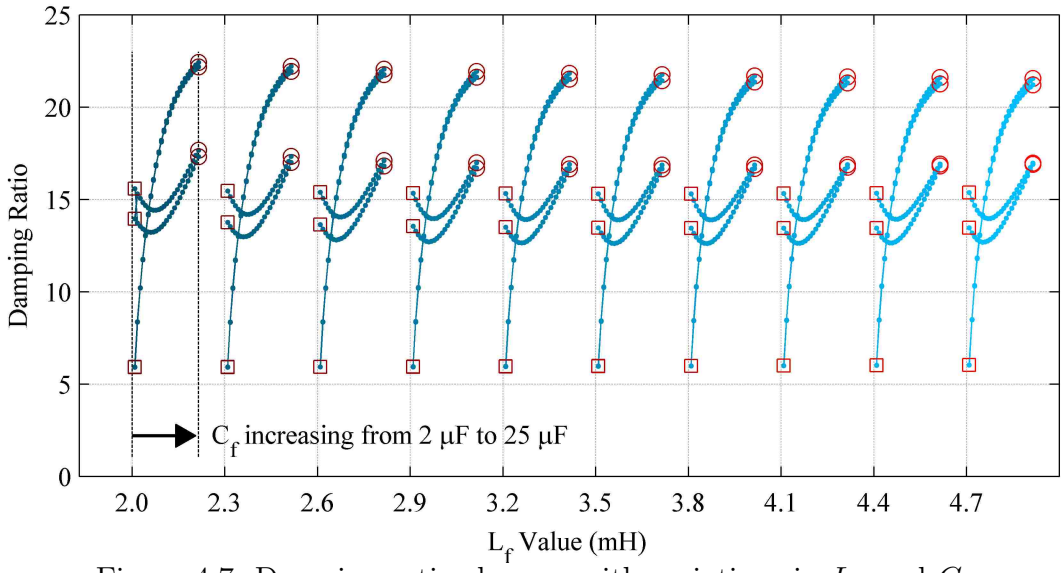

Figure 4.7 Damping ratio changes with variations in L_f and C_f

and will also cause the reactive power generated by the filter capacitors to become unacceptably large.

The main benefit of designing the LCL filter with the aid of these eigenvalue relationships is that the effects of hardware changes on the system as a whole can be observed. This is not a substitute for a design procedure such as what is given in [9], but can be a helpful resource for determining the best possible configuration within the range of possibilities that such a procedure provides.

4.2.2. Controller Design. While the eigenvalue movements with changes in L_f and C_f are relatively predictable, the changes due to selection of controller gains are much more complex. The typical methods of tuning gains are difficult to apply to this system (and other inverter controllers as well) because of the coupling between direct and quadrature axes and the cascaded structure of the control system. Often in inverter modeling research the method of determining gains is simply not discussed at all. Given the availability and accuracy of simulation programs like PLECS, it is possible to tune controller gains through trial and error until the desired response is achieved. This approach is not ideal, however, because it is time consuming and can provide results that are confusing and difficult to interpret.

As an example, consider the problem mode in the low frequency eigenvalues. From the participation factor analysis, it is known that this mode is related to the

d-axis quantities and controllers. By varying the proportional and integral gain of the d-axis current controller, the position of this eigenvalue moves in a complex semi-circular path. This is shown in Figure 4.8. In these plots, the proportional gain is incremented logarithmically from 10^0 to 10^1 and integral gain from 10^0 to $10^{2.5}$. Proportional gain changes are indicated by marker and line brightness from lightest to darkest and integral gain sweeps begin with a square marker and end with a circle. Subplot (c) most clearly shows the counterclockwise path taken by the eigenvalue with increasing integral gain. For the low values of proportional gain, the eigenvalue crosses the imaginary axis over a certain range of integral gains. As integral gain increases, however, the eigenvalue returns to the left-half-plane and converges on a similar location regardless of proportional gain. This demonstrates the difficulty involved in the trial-and-error method of gain tuning. If two simulations are run with proportional gains of 1 and integral gains of 1 and 2 for the first and second simulation respectively, the second will appear to be less stable than the first because the eigenvalue will have moved towards the imaginary axis. The logical conclusion from this comparison is that further increases in integral gain will lead to instability. In reality, the performance of the system is significantly improved by increasing the integral gain. At the very least, this sort of eigenvalue assessment provides important context for selections of gains.

Subplot (a) of Figure 4.8 shows that in addition to affecting the low frequency problem mode, one of the higher frequency modes is affected as well. As proportional gain increases, one of the eigenvalue pairs with imaginary component of ± 4000 Rad/s is pushed further into the left-half-plane, effectively increasing its damping ratio. The effect of changes in integral gain is negligible and not visible at this scale. This mode is a member of the set of problem eigenvalues previously discussed. In Section 4.1, it was shown that this mode is largely inherited from the grid-forming unit. However, as evidenced by the participation factor chart in Figure 4.2, this mode is participated in by the filter current i_{ld} and is, consequently, related to the d-axis current controller. By increasing the proportional gain of this controller, it is possible to damp the higher frequency resonance. The amount of increase in damping ratio is shown in Figure 4.9. Increasing the proportional gain to 10 provides a more significant increase in damping than any of the potential filter hardware changes. Figure 4.9 also

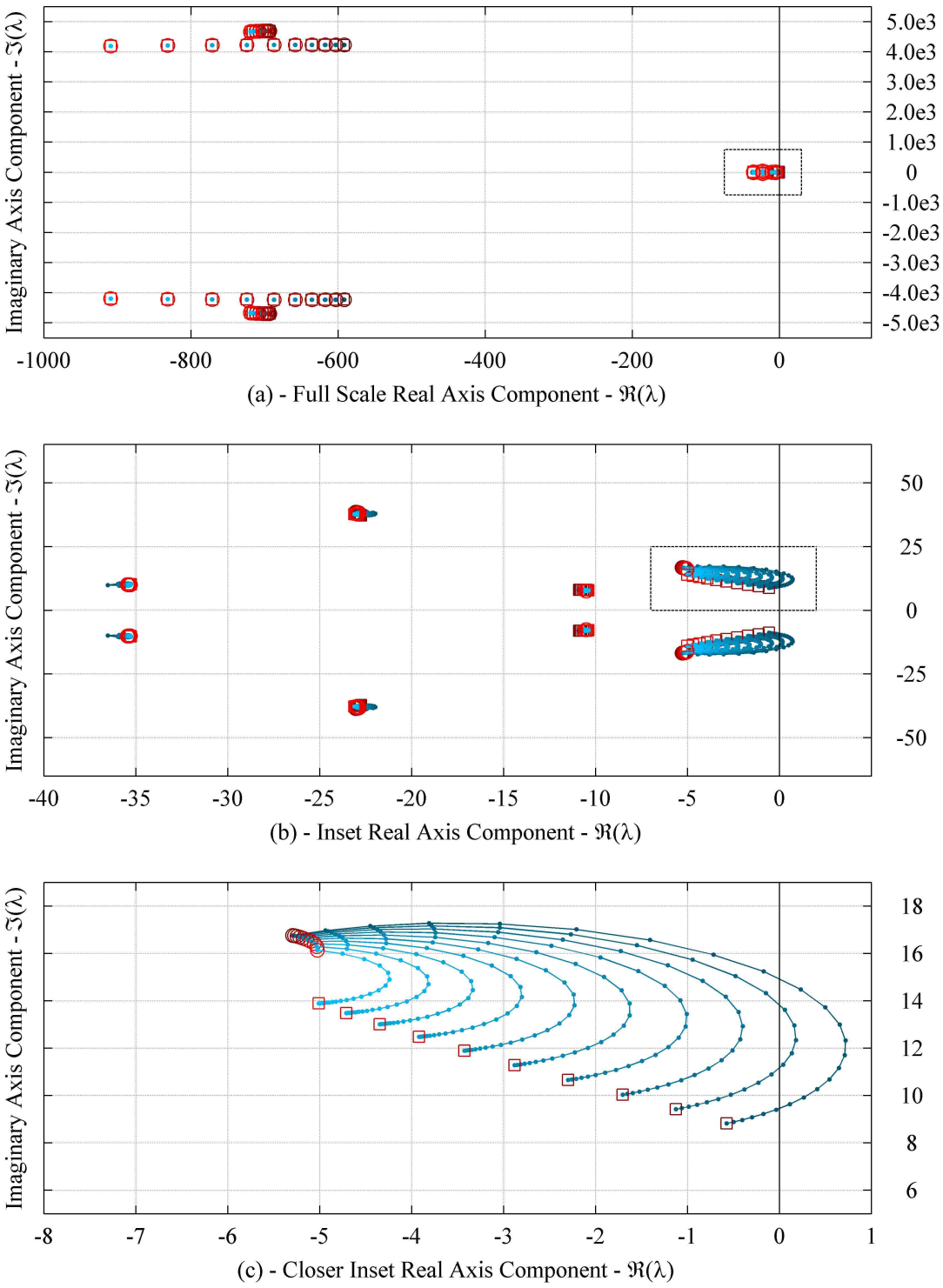

Figure 4.8 Eigenvalue position movement with increases in d-axis current controller proportional and integral gain

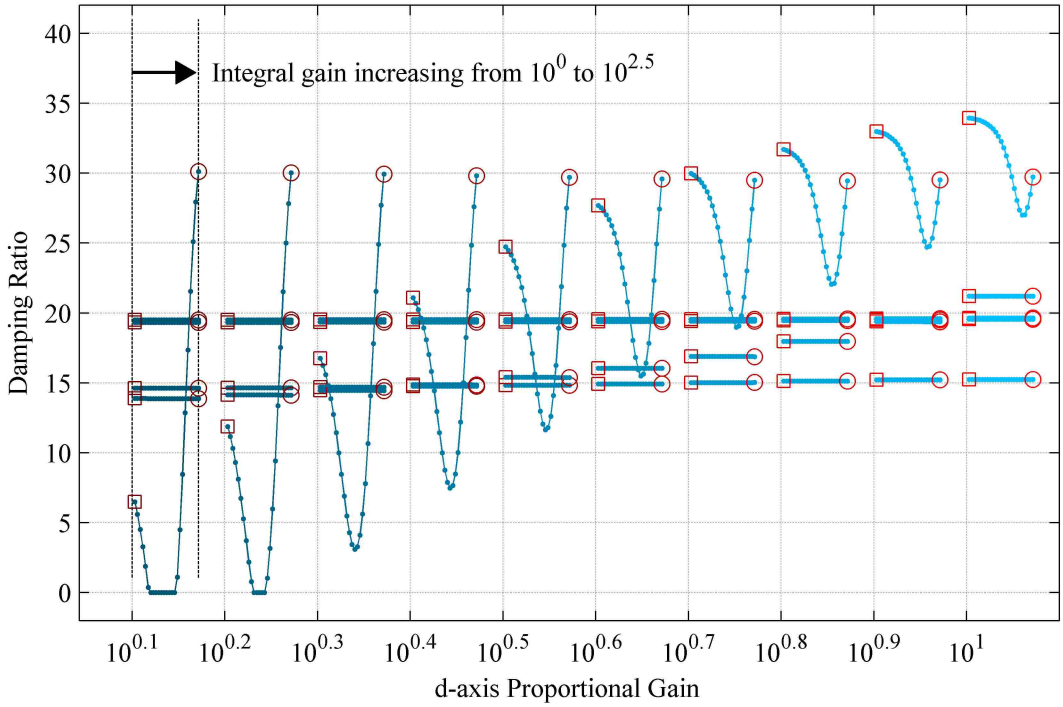

Figure 4.9 Damping ratio changes with variations in d-axis current controller gains

shows the damping ratio changes corresponding to the complex movement of the low frequency eigenvalues.

The effects of changing q-axis controller gains may be similarly assessed. Figure 4.10 shows the eigenvalue movement according to the same gain ranges and plot structure as Figure 4.8. Subplot (a) shows that increased proportional gain has a similar effect on higher frequency eigenvalues as for the d-axis current controller. Subplots (b) and (c) show the movement of the low frequency eigenvalues. Though the same range of gains is used, the range of eigenvalue movement is much more significant. The effect of increased integral gain is similar in initial semicircular shape, but at higher gains the eigenvalues do not converge as for the d-axis controller, but rather become increasingly dispersed. This again demonstrates the difficulties of gain tuning, as any insights gained from a trial-and-error approach to the d-axis controller will not apply to the q-axis. The changes in damping ratio resulting from the eigenvalue changes are shown in Figure 4.11. The lowest damping ratio corresponds to the d-axis controller, which is held at the gains used in the experiment.

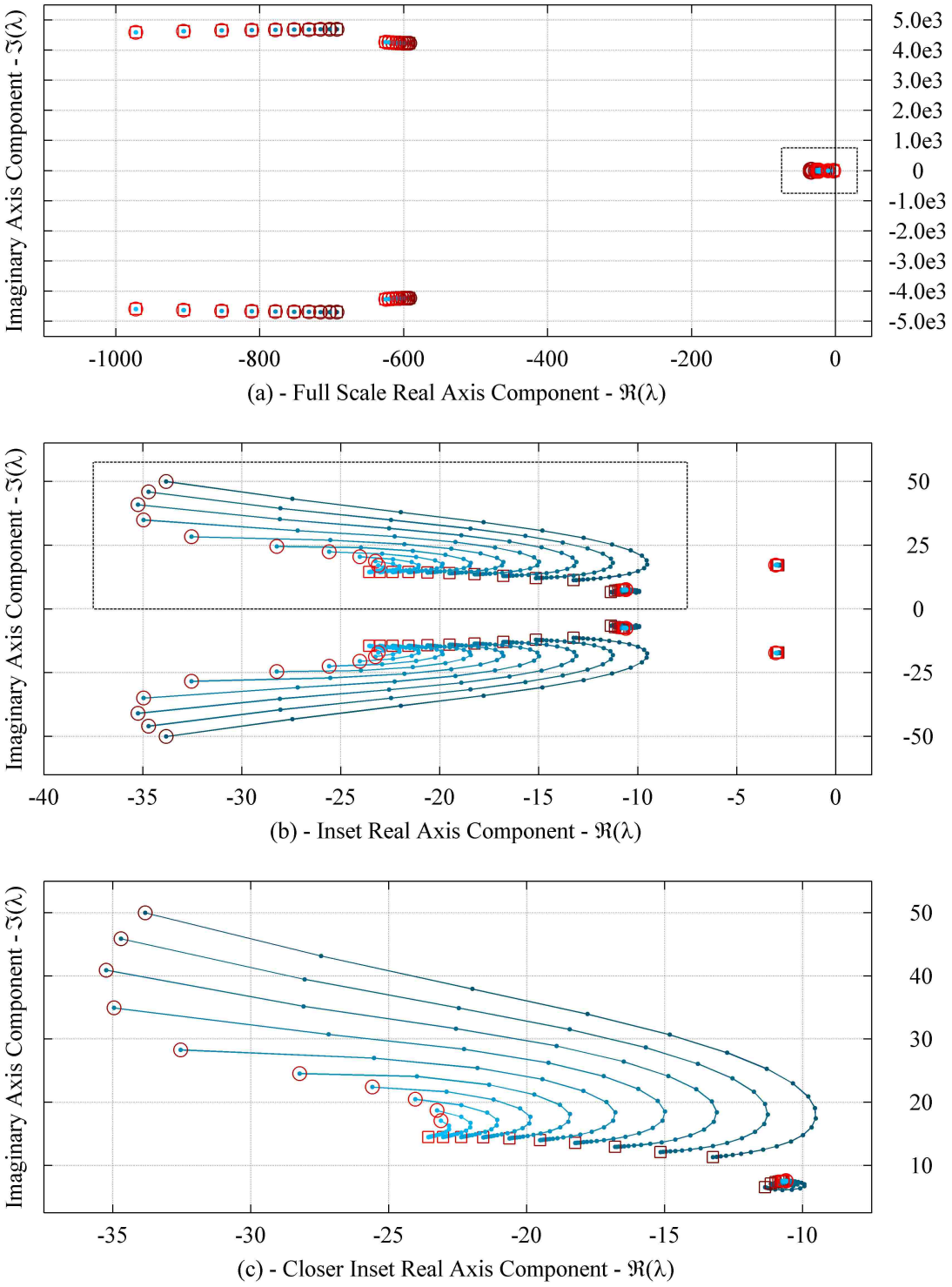

Figure 4.10 Eigenvalue position movement with increases in q-axis current controller proportional and integral gain

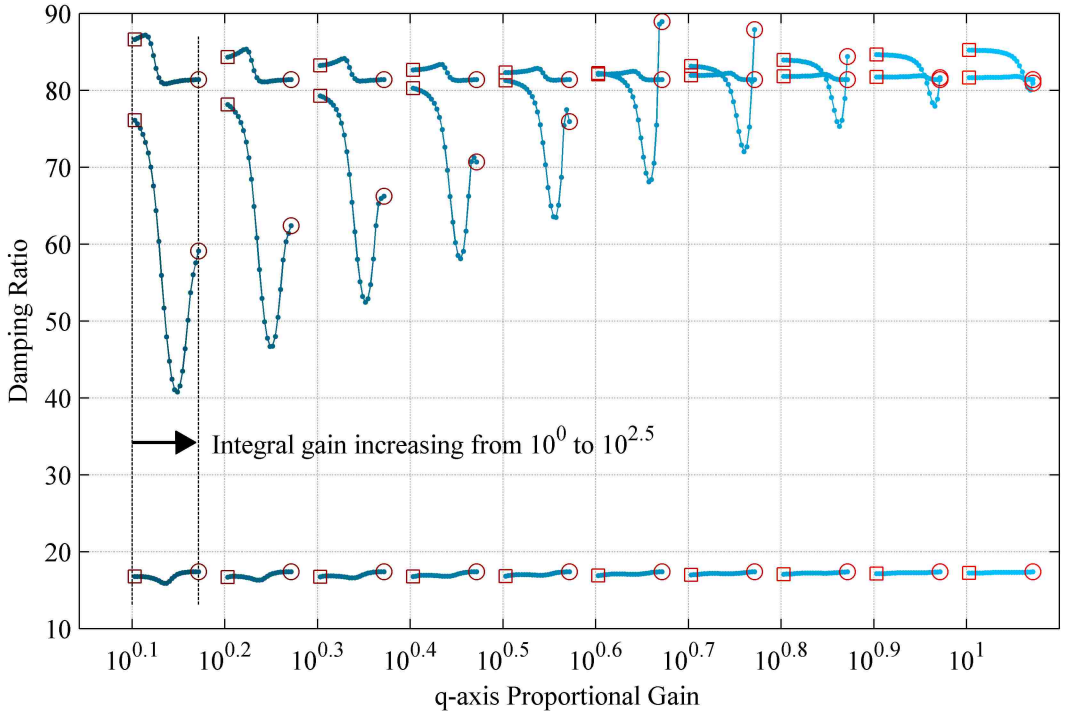

Figure 4.11 Damping ratio changes with variations in q-axis current controller gains

While this eigenvalue-based approach to choosing controller gains provides useful insights into system-wide effects of parameter changes, the range over which the gain parameters are allowed to vary must be limited. The limits should come from a more physically motivated method of analysis. For example, the increased damping resulting from high current controller proportional gains are attractive, but increasing gain beyond 10 will cause the system to be dangerously sensitive to noise in the filter current sensor path. High proportional gains also can cause the commanded voltages sent to the SVPWM to exceed maximum voltage limits, which are dependent on DC link voltage. The mode of operation in which the output voltage saturates at its maximum value is highly nonlinear and its operation is not represented by the linearized model. It is possible to select gains based eigenvalue position, determine expected dynamic response using the new model, and compare the response to the known limitations of the physical system. The most appropriate application of the eigenvalue analysis and design discussed here is as a tool to maximize the performance

of a system within a predetermined set of limitations and to determine internal relationships that may aid the design process. The relationships between parameters and eigenvalue locations discussed here are not fully generalizable because they depend on the outermost loop, which in this system is a generic placeholder for control loops designed around specific goals. However, the approach remains the same regardless of the control system, and is applicable to any grid-tied system for which a linearized model can be derived. These systems will also have their own physical limitations from which parametric boundaries must be established.

4.3. RESULTS OF DESIGN

As a basic example of the intended application of the combined model, the performance of the experimental system is improved using the eigenvalue-based design process discussed in the previous section. The results of the Q^* step change, as shown in Figure 3.4, demonstrate the poor damping of the low frequency mode related to the d-axis current controller. By setting a minimum damping ratio requirement of 30% for the low frequency eigenvalues and applying gain changes based on the relationships observed in the preceding section, the oscillation clearly visible in Figure 3.4 can be significantly reduced.

The necessary changes to the system are limited to the gains of the current controllers. The range of gains for which the damping ratio requirement is satisfied may be determined by referring back to Figures 4.9 and 4.11. There are multiple combinations of gains for which the condition is met. For the d-axis controller a damping ratio of 30% can be achieved by increasing the integral gain alone, but increasing proportional gain provides damping benefits to the higher frequency eigenvalues as well. A proportional gain of $10^{0.6}$ and integral gain of $10^{2.5}$ provides a suitable damping ratio.

For the q-axis controller, it must first be established that the relationships previously discussed hold true after the d-axis controller gains have changed. The eigenvalues related to the q-axis controller are visible in the plots of the d-axis gain sweep in Figure 4.8. Subplot (b) most clearly shows that as d-axis gains change the eigenvalues related to the q-axis controller remain relatively unchanged. Figure 4.10 shows

that for proportional gains in the middle of the range of gains observed, the trajectory of eigenvalues with increasing integral gain is nearly horizontal along the real axis. Given this relationship, it is possible to pick a q-axis proportional gain, hold the d-axis controller gains constant, and increase the q-axis integral gain until the desired damping ratio is achieved. This results in the gains shown in Table 4.2, which also provides a comparison of the eigenvalue locations and damping ratios before and after tuning the controller gains.

The most important result shown in Table 4.2 is that the damping of the low frequency mode has been successfully increased to greater than 30%. The damping of all problem modes increases, but the increases seen by the higher frequency modes are less significant. The eigenvalue related to the q-axis controller, though not identified as a problem mode, increases in damping from 50.12% to 73.89%.

To verify the beneficial effects these gain changes, the Q^* step change experiment is repeated with the newly tuned controllers. The results of this test are shown in Figures 4.12 and 4.13. The model is again accurate and the low frequency oscillations

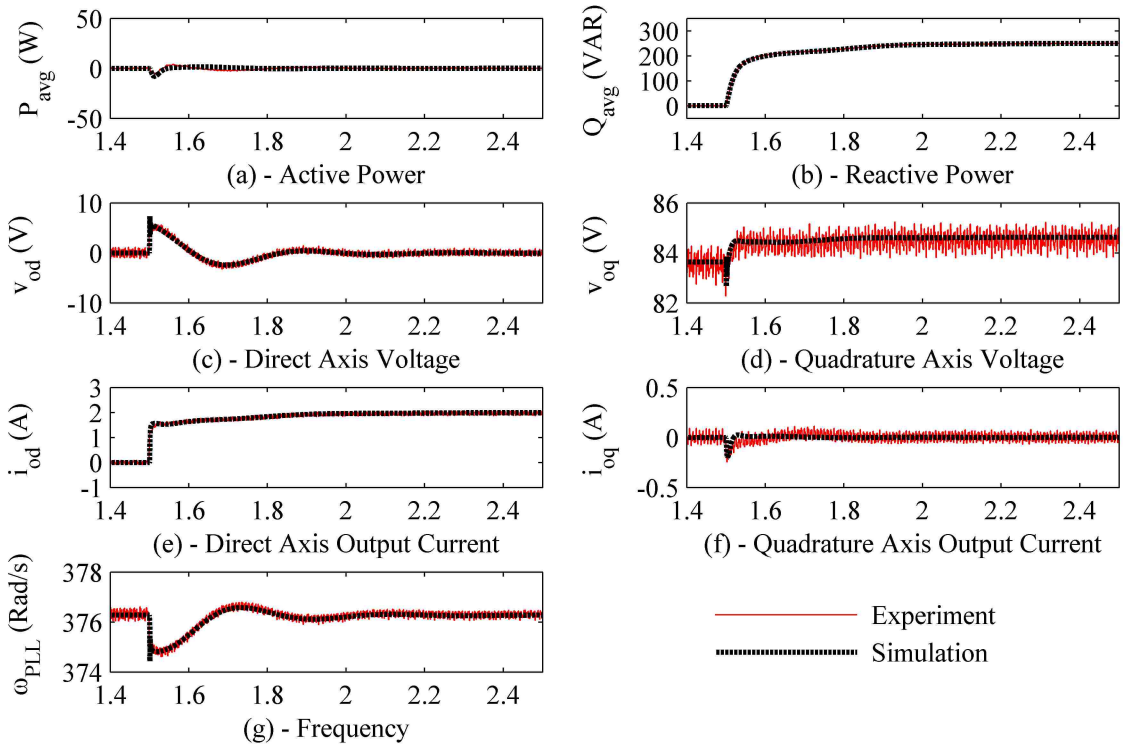

Figure 4.12 Q^* step change after tuning controller gains

visible in the previous Q^* step change test are dramatically reduced. Figure 4.13 provides a more clear perspective of the magnitude of the change. This is an important result, because the autonomous grid-forming units in droop-controlled microgrids are susceptible to oscillation in bus voltage and frequency as they approach equal power sharing. This model is able to identify areas in which oscillation may occur in the dynamics of parallel inverters, determine which parameters influence these oscillations, and accurately predict the system response if these parameters are changed.

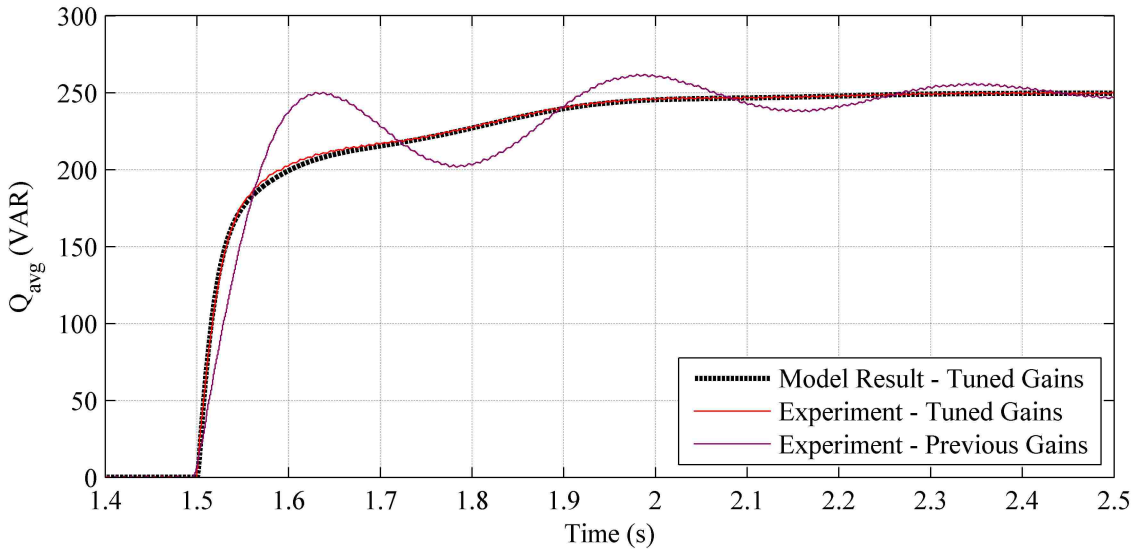

Figure 4.13 Q^* step response before and after tuning controller gains

Table 4.2 Eigenvalues and damping ratios before and after tuning gains

Original Gains			**Tuned Gains**		
kp_{id}	1		kp_{id}	4	
ki_{id}	100		ki_{id}	350	
kp_{iq}	1		kp_{iq}	2	
ki_{iq}	100		ki_{iq}	500	
$\mathfrak{R}(\lambda)$	$\mathfrak{S}(\lambda)$	ζ	$\mathfrak{R}(\lambda)$	$\mathfrak{S}(\lambda)$	ζ
-2.03×10^8	± 376.29	100	-2.03×10^8	± 376.29	100
-2.47×10^3	$\pm 1.24 \times 10^4$	19.51	-2.47×10^3	$\pm 1.25 \times 10^4$	19.59
-2.31×10^3	$\pm 1.17 \times 10^4$	19.32	-2.31×10^3	$\pm 1.17 \times 10^4$	19.44
-7.96×10^3	0	100	-7.96×10^3	0	100
-692.85	$\pm 4.69 \times 10^3$	14.62	-749.81	$\pm 4.69 \times 10^3$	15.80
-591.91	$\pm 4.23 \times 10^3$	13.87	-732.17	$\pm 4.23 \times 10^3$	17.06
-834.76	± 281.6	94.76	-832.17	± 307.73	93.80
-516.52	± 20.963	99.92	-860.91	0	100
			-521.17	0	100
-21.972	± 37.935	50.12	-85.318	± 77.815	73.89
-45.296	± 24.554	87.91	-67.278	± 31.435	90.60
-49.725	0	100	-49.790	0	100
-50.248	0	100	-50.247	0	100
-35.403	± 9.795	96.38	-26.806	± 14.136	85.46
-3.040	± 17.249	17.36	-5.515	± 16.360	31.94
-10.589	± 7.576	81.33	-10.515	± 7.591	81.08
-6.205	± 0.926	98.40	-6.7334	0	100
			-6.198	0	100
-5.794	0	100	5.852	0	100
0	0	100	0	0	100

5. CONCLUSIONS

Though inverter modeling is a thoroughly researched and well understood topic, the context in which an inverter is used significantly influences the applicability of the models used in its design. In this thesis it is shown that a grid-tied inverter model, while accurate, is insufficient as a tool for designing similarly functioning inverters in microgrids. The reason for this inadequacy is the presence of voltage and frequency variations at the point of connection to the microgrid. While voltage and frequency may be successfully assumed to be fixed in the development of a grid-tied inverter, variations in these parameters occur during nominal operation of an islanded microgrid, and must therefore be considered in the design process of an inverter to be connected to such a system. The disparity between the grid-tied and grid-supporting inverter responses is illustrated by the comparison of the Q^* step changes. The controller gains used to produce a satisfactory response in grid-tied operation result in an underdamped response when used in a grid-supporting context. In cases such as this, improper design may threaten the stability of the microgrid as a whole. Even if the consequences are not so dire, the fact that the system response cannot be accurately predicted by existing models indicates the need for a model adaption technique, and motivates the work in this thesis.

In order to properly describe the behavior of a grid-supporting unit, regardless of its specific function, a model capable of representing the coupling between complex power, frequency, and bus voltage is required. The combined model presented here satisfies all of these requirements. The model consists of both a grid-supporting and a grid-forming inverter, each with their own individually derived small-signal model. The transformation from grid-tied model to grid-supporting model is accomplished through the use of the virtual resistor at the grid-forming unit's output. The changes in voltage at this point, which follow the P/f and Q/V droop control laws, are used as disturbance inputs by the grid-supporting model. The full model is shown to be accurate in its predictions of the step responses for active and reactive power commands.

In addition to the prediction of dynamic response, the linear state-space form of the model allows established analysis methods to be used to characterize the system's behavior. An eigenvalue analysis is an example of such a method. Observing the changes in eigenvalues before and after the models are combined provides insight into the nature of the interactions between inverter control systems. The eigenvalue analysis is shown to be an effective tool for tuning the response of the system. By observing the relationships between eigenvalue movements and changes in parameters, response characteristics may be shaped in a straightforward and analytic manner. Above all, this aids in the remediation of problem resonances. This is an important result, because these issue may be present in a power system composed of low inertia droop controlled sources but absent from a traditional stiff grid, and therefore not within the scope of existing inverter models.

While the specific system analyses performed here cannot be extended to all grid-supporting inverters, the general procedure is applicable to any externally controlled inverter designed around a specific set of operational goals. If an inverter control system can be modeled in a synchronous reference frame and linearized at a nominal bus voltage and frequency around which small variations occur, the analysis and design methods outlined here can be applied. This is true not only for parallel grid-supporting grid-forming pairs, but for any number of parallel grid-supporting units connected to the same microgrid bus. Furthermore, the resulting system can be combined after linearization, meaning that any number of grid-supporting inverters may be designed individually before being included in the full system.

Despite the advantages of a model derived according to the procedure in this thesis, the end result is still a small-signal model subject to all the limitations of assumptions of linearity. Inescapable nonlinearities such as switching dead time, output voltage limits and current limits, and inductor saturation are beyond the capabilities of such models. When performing a stability analysis, the model may be a useful tool in consideration of the control system, but the situations most likely to cause instability do not result from linear control action. The model behavior is undefined when even one inverter of a combined system enters an output limiting mode of operation. While the combined model may be able to indicate when the

inverter will enter a limiting mode, it will not be able to say what happens next, or what can be done to return the system to nominal operation.

Within the limits of its abilities, though, the process of model combination given in this thesis provides information on inverter interactions within a microgrid that is otherwise not available using existing linearized models. This information may be used to aid the design of microgrid systems both at the local inverter level and in higher layers of control. The success of secondary, system-level control functions depends on accurate knowledge of the dynamics of the grid-supporting inverters used to execute distributed control actions. The method of describing grid-supporting inverter behavior described here is a stepping stone in the process of research and development of full microgrid control architectures.

BIBLIOGRAPHY

[1] N. Bottrell, M. Prodanovic, and T. Green. Analysed small signal state-space model of an active rectifier. In *Universities Power Engineering Conference (UPEC), 2010 45th International*, pages 1–6, Aug 2010.

[2] E. Coelho, P. Cortizo, and P. Garcia. Small-signal stability for parallel-connected inverters in stand-alone ac supply systems. *Industry Applications, IEEE Transactions on*, 38(2):533–542, Mar 2002.

[3] K. De Brabandere, B. Bolsens, J. Van den Keybus, A. Woyte, J. Driesen, and R. Belmans. A voltage and frequency droop control method for parallel inverters. *Power Electronics, IEEE Transactions on*, 22(4):1107–1115, July 2007.

[4] J. Guerrero, J. Vasquez, J. Matas, L. de Vicua, and M. Castilla. Hierarchical control of droop-controlled ac and dc microgrids;a general approach toward standardization. *Industrial Electronics, IEEE Transactions on*, 58(1):158–172, Jan 2011.

[5] F. Katiraei, M. Iravani, and P. Lehn. Small-signal dynamic model of a microgrid including conventional and electronically interfaced distributed resources. *Generation, Transmission Distribution, IET*, 1(3):369–378, May 2007.

[6] N. Kroutikova, C. Hernandez-Aramburo, and T. Green. State-space model of grid-connected inverters under current control mode. *Electric Power Applications, IET*, 1(3):329–338, May 2007.

[7] P. Kundur. *Power System Stability and Control*. McGraw-Hill, 1994.

[8] D. Lee and J. Ahn. A simple and direct dead-time effect compensation scheme in pwm-vsi. *Industry Applications, IEEE Transactions on*, PP(99):1–1, 2014.

[9] M. Liserre, F. Blaabjerg, and S. Hansen. Design and control of an lcl-filter-based three-phase active rectifier. *Industry Applications, IEEE Transactions on*, 41(5):1281–1291, Sept 2005.

[10] Z. Liu, J. Liu, and Y. Zhao. A unified control strategy for three-phase inverter in distributed generation. *Power Electronics, IEEE Transactions on*, 29(3):1176–1191, March 2014.

[11] R. Majumder. Some aspects of stability in microgrids. *Power Systems, IEEE Transactions on*, 28(3):3243–3252, Aug 2013.

[12] R. Majumder, A. Ghosh, G. Ledwich, and F. Zare. Stability analysis and control of multiple converter based autonomous microgrid. In *Control and Automation, 2009. ICCA 2009. IEEE International Conference on*, pages 1663–1668, Dec 2009.

[13] E. Planas, A. Gil-de Muro, J. Andreu, I. Kortabarria, and I. Martinez de Alegria. Design and implementation of a droop control in d-q frame for islanded microgrids. *Renewable Power Generation, IET*, 7(5):458–474, Sept 2013.

[14] N. Pogaku, M. Prodanovic, and T. Green. Modeling, analysis and testing of autonomous operation of an inverter-based microgrid. *Power Electronics, IEEE Transactions on*, 22(2):613–625, March 2007.

[15] M. Prodanovic and T. Green. Control and filter design of three-phase inverters for high power quality grid connection. *Power Electronics, IEEE Transactions on*, 18(1):373–380, Jan 2003.

[16] M. Rasheduzzaman, J. Mueller, and J. Kimball. An accurate small-signal model of inverter-dominated islanded microgrids using dq reference frame. *Emerging and Selected Topics in Power Electronics, IEEE Journal of*, PP(99):1–1, 2014.

[17] M. Rasheduzzaman, J. Mueller, and J. Kimball. Small-signal modeling of a three-phase isolated inverter with both voltage and frequency droop control. In *Applied Power Electronics Conference and Exposition (APEC), 2014 Twenty-Ninth Annual IEEE*, pages 1008–1015, March 2014.

[18] J. Rocabert, A. Luna, F. Blaabjerg, and P. Rodriguez. Control of power converters in ac microgrids. *Power Electronics, IEEE Transactions on*, 27(11):4734–4749, Nov 2012.

[19] P. Shamsi and B. Fahimi. Dynamic behavior of multiport power electronic interface under source/load disturbances. *Industrial Electronics, IEEE Transactions on*, 60(10):4500–4511, Oct 2013.

[20] X. Tang, W. Deng, and Z. Qi. Investigation of the dynamic stability of microgrid. *Power Systems, IEEE Transactions on*, 29(2):698–706, March 2014.

[21] E. Twining and D. Holmes. Grid current regulation of a three-phase voltage source inverter with an lcl input filter. *Power Electronics, IEEE Transactions on*, 18(3):888–895, May 2003.

[22] J. Uudrill. Dynamic stability calculations for an arbitrary number of interconnected synchronous machines. *Power Apparatus and Systems, IEEE Transactions on*, PAS-87(3):835–844, March 1968.

[23] T. Vandoorn, J. Vasquez, J. De Kooning, J. Guerrero, and L. Vandevelde. Microgrids: Hierarchical control and an overview of the control and reserve management strategies. *Industrial Electronics Magazine, IEEE*, 7(4):42–55, Dec 2013.

VITA

Jacob Andreas Mueller was born in St. Louis, Missouri. He received the Bachelor of Science degrees in Electrical and Computer Engineering from Missouri University of Science and Technology in 2012. In 2014 he received the Master of Science degree in Electrical Engineering, also from Missouri S&T.